The Journal of Physiology



# Properties of rhythmogenic currents in spinal Shox2 interneurons across postnatal development

Shayna Singh, Natalia A. Shevtsova, Lihua Yao, Ilya A. Rybak and Kimberly J. Dougherty

*Marion Murray Spinal Cord Research Center, Department of Neurobiology and Anatomy, Drexel University College of Medicine, Philadelphia, PA, USA*

Handling Editors: Nathan Schoppa & Vatsala Thirumalai

The peer review history is available in the Supporting Information section of this article (https://doi.org/10.1113/JP287752#support-information-section).

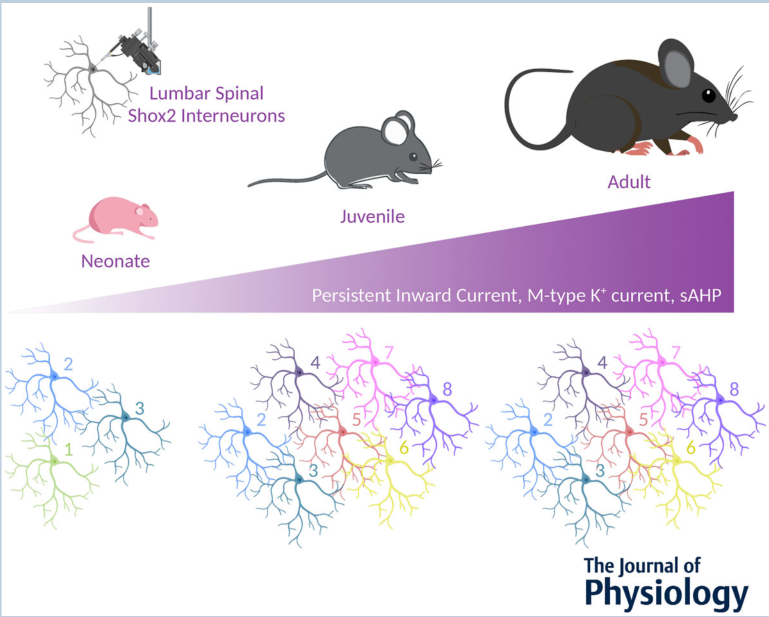


**Abstract figure legend** Rhythm is an essential feature of mature locomotor behaviour, and it is encoded by spinal interneurons. We utilized lumbar spinal Shox2 interneurons as a representative population of rhythmgenerating neurons to investigate how putatively rhythmogenic conductances develop with postnatal age. Juvenile and adult mice, which perform weight-bearing stepping, show increased diversity of intrinsic properties measured using whole cell patch clamp compared to Shox2 interneurons from neonatal mice. We predict that there is strong interplay between the enhanced conductances we identified in mature Shox2 INs, and we suggest that these conductances are employed dynamically to shape and maintain robust rhythmic behaviour.

**Shayna Singh** received her Bachelor's degree in biological sciences in 2019 from Drexel University. Her PhD has focused on the intrinsic properties of and descending connections to spinal Shox2 interneurons in the context of locomotion. She aims to continue researching motor physiology beyond her PhD. When she is not at the patch rig, she can be found on the microscope looking at the neurons that she uses electricity to talk to. She values the combination of physiology and anatomy in her examinations of the nervous system.

This article was first published as a preprint. Singh S, Yao L, Shevtsova NA, Rybak IA, Dougherty KJ. 2024. Properties of rhythmogenic currents in spinal Shox2 interneurons across postnatal development. bioRxiv. https://doi.org/10.1101/2024.09.26.612677

 DOI: 10.1113/JP287752

**Abstract** Locomotor behaviours are performed by organisms throughout life, despite developmental changes in cellular properties, neural connectivity and biomechanics. The basic rhythmic activity in the central nervous system underlying locomotion is considered to be generated via a complex interplay between network and intrinsic cellular properties. Within mature mammalian spinal locomotor circuitry, we have yet to determine which properties of spinal interneurons (INs) are critical to rhythmogenesis and how they change during development. Here, we combined whole cell patch clamp recordings, immunohistochemistry and RNAscope targeting lumbar Shox2 INs in mice, which are known to be involved in locomotor rhythm generation. Our goal was to determine the postnatal developmental expression of voltage-sensitive conductances, in addition to respective ion channels, in Shox2 INs. We show that subsets of Shox2 INs display persistent inward currents, M-type potassium currents, slow afterhyperpolarization and T-type calcium currents, which are enhanced with age. By contrast, the hyperpolarization-activated and A-type potassium currents were either found with low prevalence in subsets of neonatal, juvenile, and adult Shox2 INs or did not developmentally change. We show that Shox2 INs become more electrophysiologically diverse by juvenile and adult ages, when locomotor behaviour becomes weight-bearing. Computational modelling was used to simulate and reproduce electrophysiological experiments for representative Shox2 INs to make predictions regarding the interactions between experimentally recorded conductances and persistent inward currents, and bursting behaviour. Our results suggest a developmental shift in the magnitude of rhythmogenic ionic currents and the expression of corresponding ion channels that may be important for mature locomotor behaviour.

(Received 26 September 2024; accepted after revision 3 April 2025; first published online 2 May 2025)
**Corresponding author** K. J. Dougherty: Department of Neurobiology and Anatomy, Drexel University College of Medicine, 2900 Queen Lane, Philadelphia, PA, 19129, USA. Email: kjd86@drexel.edu

**Key points**

- The intrinsic and voltage-sensitive properties of locomotor-related neurons contribute to shaping and maintaining activity.
- Shox2 interneurons (INs), similar to many other components of locomotor circuitry, are well-characterized in the neonatal mouse.
- Electrophysiological recordings reveal that subsets of Shox2 INs express ‘rhythmogenic properties’, including persistent inward currents, M-type potassium currents and slow after-hyperpolarization, as well as corresponding ion channels/RNA.
- Hierarchical clustering demonstrates that developmental changes seen are related to the emergence of electrophysiological cell types, largely defined by strong rhythmogenic current expression.
- Our data suggest that Shox2 INs gain electrophysiological diversity with age, and that Shox2 INs from adult mice may employ enhanced voltage-sensitive conductances during rhythmic locomotor activity.

## Introduction

Rhythm generation is an essential function of the nervous system. Rhythmic neuronal firing is vital to nutrient intake (Marder & Calabrese, 1996; Spencer et al., 2018), waste expulsion (Bywater et al., 1989), breathing (Feldman, 1986) and locomotion (Dougherty & Ha, 2019). Aberrant neuronal rhythms also arise in pathologies, such as in neuropathic pain (Amir et al., 1999) and Parkinson’s disease (Oswal et al., 2013). Within rhythmic motor behaviours including mastication, respiration and locomotion, neurons employ rhythmogenic network and intrinsic properties to encode the timing of motor output (Harris-Warrick, 2010). In the spinal cord, the locomotor central pattern generator (CPG) includes dedicated neurons for rhythmic locomotor output (McCrea & Rybak, 2008). Neonatal rodents have been used in many studies of neurons involved in locomotor circuitry as a result of transgenic neuronal targeting and the ability to evoke fictive locomotor activity in reduced neonatal preparations (Cazalets et al., 1996; Cowley & Schmidt, 1997; Dougherty et al., 2013; Kjaerulff & Kiehn, 1996; Ziskind-Conhaim et al., 2010). Although capable of producing locomotor-like behaviour, the neonatal spinal cord is immature in its cellular and synaptic properties (Borowska et al., 2015; Chang et al., 1999; Ha & Dougherty, 2018; Sharples & Miles, 2021). However, despite developmental changes within the spinal locomotor CPG, locomotor rhythm generating neurons are considered to remain rhythmogenic throughout the life of the animal. Whether significant changes developmentally occur in the intrinsic rhythmogenic properties of locomotor CPG neurons is beginning to be explored (Husch et al., 2015).

Spinal Shox2 interneurons (INs) are a putative rhythm-generating population in the mouse spinal cord (Dougherty et al., 2013) and are positioned to be rhythm-generating in that they are ventromedially located, excitatory and form mutual connections (Brownstone & Wilson, 2008; Dougherty et al., 2013, Ha & Dougherty, 2018). Furthermore, silencing these neurons decreases the frequency of locomotor-like activity in the isolated neonatal spinal cord (Dougherty et al., 2013). Previous work has shown that neonatal Shox2 INs are highly interconnected by gap junctional coupling, with decreasing prevalence as the mouse ages (Ha & Dougherty, 2018). Rhythmicity is evident in neonatal Shox2 INs during fictive locomotion (Dougherty et al., 2013) but, in the adult spinal slice, where network connections are limited to those that are local within the slice, a small subset of Shox2 INs display spontaneous oscillations (Garcia-Ramirez et al., 2021). These findings indicate that Shox2 INs are rhythmogenic even within a limited network and potentially employ intrinsic rhythmogenic properties which change with age. Although lumbar spinal Shox2 INs represent a heterogeneous population (Garcia-Ramirez et al., 2022) and are not the only locomotor-related rhythmogenic neuron type (Bertho et al., 2024; Chalif et al., 2022; Ziskind-Conhaim et al., 2010), we use them in the present study as a representative neuronal population for rhythmogenic spinal CPG neurons.

Rhythmicity of CPG neurons, as in many other rhythmogenic neuron types across the nervous system, is maintained and shaped, at least in part, by potentially rhythmogenic ionic currents (Harris-Warrick, 2010). These include slowly inactivating inward currents which maintain the sustained depolarization needed for burst firing, such as persistent inward currents (PICs), hyperpolarization-activated current ($I_H$) and T-type calcium current ($I_T$) (Harris-Warrick, 2002, 2010; Verneuil et al., 2020). To balance this, outward or hyperpolarizing currents also shape rhythmic firing, such as slow afterhyperpolarization (sAHP) and M- ($I_M$) and A-type ($I_A$) potassium currents (Harris-Warrick, 2002, 2010; Verneuil et al., 2020). These putatively rhythmogenic currents may be employed in a myriad of combinations across different biological contexts (Alonso & Marder, 2020). Additionally, each ionic current is mediated within individual neurons by a suite of voltage-sensitive ion channels that we are beginning to understand using genetic and histological tools. Moreover, the rhythmic firing in neurons is determined by the combination of passive and active cellular properties. Within these complexities of rhythmogenic intrinsic properties, there may be future therapeutic targets for the modulation or restoration of rhythm in the spinal locomotor CPG following injury (Brocard et al., 2016). Accordingly, it is crucial to understand rhythmogenic spinal CPG neurons in adult animals, where cellular properties and connections have reached maturity.

In the present study, we sought to determine which ionic currents are present in Shox2 INs and how they change with postnatal development in mice. Using whole-cell patch clamp electrophysiology, we found that all examined putatively-rhythmogenic currents are present in small or large subsets of Shox2 INs. Strong PICs which persist onto the descending phase of a symmetrical voltage ramp and sAHPs are largely absent in Shox2 INs from neonatal mice. We found that $I_M$, similar to PICs, increases in magnitude with age. Furthermore, subsets of Shox2 INs across postnatal development express channels that are known to contribute to PICs, $I_M$ and sAHP. Because it is the combination of passive and active cellular properties that determine the interactions resulting in intrinsic rhythm, we performed unbiased hierarchical clustering of all measured electrophysiological parameters. This revealed electrophysiological subtypes of Shox2 INs that were age-dependent. Computational modelling was used to reproduce voltage ramp experiments for representative age-specific Shox2 IN subtypes based on clustering. These single Shox2 IN models suggest the contribution of different currents to PICs and predicted bursting behaviour in response to pharmacologically enhancing PICs in adult Shox2 INs. Taken together, experimental and modelling data suggest that the conductances present in Shox2 INs are enhanced with postnatal age, may interact dynamically and could contribute to bursting behaviour.

## Methods

### Ethical statement

All experimental procedures followed National Institutes of Health guidelines and were approved by the Institutional Animal Care and Use Committee at Drexel University (Protocols 20901 and LA-23-731). We understand and are in compliance with the animal ethical principles under which *The Journal of Physiology* operates.

## Mouse lines

All animal experiments were performed using the following transgenic mouse lines: *Shox2::Cre* (Dougherty et al., 2013); *R26-lsl-tdTomato* (Ai9 from The Jackson Laboratory; #007909) (Madisen et al., 2010); and *Shox2::Cre; R26-lsl-tdTomato;Vsx2-eGFP* (Vsx2-EGFP from Mutant Mouse Regional Resource Centre; #011391-UCD) (Gong et al., 2003). Neonatal [postnatal day (P)2–5, 7], juvenile (P14–21) and adult (P60–138) transgenic mice were used for this study. Mice were group housed under a 12:12 h light/dark photocycle, fed *ad libitum* and had unrestricted access to water.

## Slice preparation

To access lumbar spinal Shox2 INs in the spinal slice, juvenile and adult mice were first anaesthetized with ketamine (150 mg $kg^{-1}$) and xylazine (15 mg $kg^{-1}$). Following decapitation and evisceration, spinal cords were removed from all mice in ice-cold dissecting solution. The dissecting solution used for neonatal mice (P2–5) contained the following (in mM): 111 NaCl, 3 KCl, 11 glucose, 25 $NaHCO_3$, 3.7 $MgSO_4$, 1.1 $KH_2PO_4$ and 0.25 $CaCl_2$. For juvenile and adult mice, the dissection solution contained (in mM): 222 glycerol, 3 KCl, 11 glucose, 25 $NaHCO_3$, 1.3 $MgSO_4$, 1.1 $KH_2PO_4$ and 2.5 $CaCl_2$. The lumbar spinal cord (L1–5) was sectioned transversely (300 μm) in dissection solution using a vibrating microtome (Leica Microsystems, Wetzlar, Germany). Slices were immediately transferred to recording artificial cerebrospinal fluid (ACSF) containing the following (in mM): 111 NaCl, 3 KCl, 11 glucose, 25 $NaHCO_3$, 1.3 $MgSO_4$, 1.1 $KH_2PO_4$ and 2.5 $CaCl_2$. Slices from a subset of juvenile and all adult mice were incubated at 34°C for 20–30 min and then rested at room temperature for 1 h before recording. Dissecting and recording solutions were continuously aerated with 95%/5% $O_2/CO_2$.

## Electrophysiological recordings

Fluorescently labelled tdTomato$^+$ Shox2 INs were visualized with a 63× objective lens on a BX51WI scope (Olympus, Tokyo, Japan) using LED illumination (X-Cite; Lumen Dynamics, Mississauga, ON, Canada) and targeted for whole-cell patch clamp recordings. Electrodes were pulled to tip resistances of 5–12 MΩ using a multistage puller (Sutter Instruments, Novato, CA, USA) and were filled with intracellular solution which contained (in mM): 128 K-gluconate, 10 HEPES, 0.0001 $CaCl_2$, 1 glucose, 4 NaCl, 5 ATP and 0.3 GTP. In experiments using riluzole or nimodipine, a cesium-based intracellular solution was used, containing (in mM): 130 $CsMeSO_3$, 10 HEPES, 0.5 EGTA, 2 $MgCl_2$, 2 ATP and 5 CsCl. In some experiments, biocytin (2 mg $mL^{-1}$; Sigma, St Louis, MO, USA) was included in the patch electrode. All recordings were performed at room temperature. Data were collected with a Multiclamp 700B amplifier (Molecular Devices, San Jose, CA, USA) and Clampex software (pClamp9; Molecular Devices). Signals were digitized at 20 kHz and filtered at 6 kHz. Measurements were collected and calculated from recording traces in Clampfit 11 (Clampex; Molecular Devices).

## Electrophysiological data collection and analysis

Resting membrane potential was recorded shortly after gaining whole-cell access. Recordings in current clamp were taken using current steps when holding the cell near −65 mV via injecting bias current. Input resistance was calculated from the current/voltage slope in response to hyperpolarizing current steps in which no voltage-gated current activation was present. Time constant was measured as the duration of time to reach 63% of the maximum membrane voltage change in response to a hyperpolarizing current step. Input capacitance was calculated by dividing input resistance by time constant. Leak conductance was calculated as the inverse of the input resistance. Action potential properties (threshold, rheobase, sAHP duration and sAHP amplitude) were measured from the first spike elicited from the depolarizing current step at rheobase. Voltage-sensitive currents were isolated in voltage clamp mode. To record PICs, cells were held at −80 mV and subjected to three sequential symmetrical voltage ramps in which the cells were brought to −10 mV in 2.5 s, and back down to −80 mV in 2.5 s (Dai & Jordan, 2010). Measurements including PIC onset, area of the current and maximum amplitudes were taken from the first voltage ramp. To isolate and measure $I_H$, cells were subjected to a 500 ms hyperpolarizing step from −60 mV to −140 mV. Occasionally, a cell would not return to steady state within the 500 ms duration, so 1 s steps were performed in addition. To record and measure $I_T$ and $I_A$, cells were subjected to two sequential 250 ms depolarizing steps to −30 mV; the first was from −100 mV to deinactivate the relevant channels and the second from −60 mV. Measurements were taken from the voltage step that the current was maximally activated by. The tail relaxation curve of $I_M$ was measured from recordings of cells hyperpolarized to −60 mV from an initial holding of −10 mV (Brown & Adams, 1980). Current magnitudes are reported as current density, where the maximum amplitude of the current is normalized by the cell's input capacitance.

## Pharmacology

The following pharmacological agents were used in this study: 10 μM riluzole (R116; Sigma), 20 μM nimodipine (N149; Sigma), 10 μM XE991 (X2254; Sigma), 100 nM apamin (A1289; Sigma) and 200 nM veratridine (676950M; Sigma). All were dissolved in recording ACSF except for riluzole, which was dissolved in dimethyl sulphoxide and subsequently added to recording ACSF. The final concentration of dimethyl sulphoxide was 0.05%.

## Immunohistochemistry and RNAscope *in situ* hybridization

*Shox2::Cre;lsl-tdTomato* mice at P14 and P64 were anaesthetized with ketamine (150 mg $kg^{-1}$) and xylazine (15 mg $kg^{-1}$) and perfused transcardially with 0.1 M PBS, followed by 4% paraformaldehyde in PBS. *Shox2::Cre; R26-lsl-tdTomato* mice at P2 and P7 were decapitated and eviscerated in PBS. Spinal cords were harvested from each animal and fixed overnight in 4% paraformaldehyde solution at 4°C. Fixed spinal cords were subsequently maintained in 30% sucrose in PBS for at least 48 h. Tissue was then embedded in OCT compound (Thermo Fisher Scientific, Waltham, MA, USA) over dry ice and stored at −80°C. Lumbar spinal cords were sectioned (20 μm) transversely on a cryostat (HM 505 E; Microm International GmbH, Walldorf, Germany) and directly mounted onto coated (immunohistochemistry) or charged (RNAscope, Advanced Cell Diagnostics, Newark, CA, USA) slides. Slides were washed in PBS before being used for immunohistochemistry or RNAscope.

For immunohistochemistry, slides were first blocked in a PBS solution containing 5% goat serum, 1% bovine serum albumin, 0.2% Triton X-100 and 0.1% fish gelatin. Slides were incubated in one of the following primary antibodies overnight: rabbit anti-KCNQ2 (dilution 1:1000; PA1-929; Thermo Fisher Scientific), rabbit anti-KCNQ3 (dilution 1:400; APC-051; Alomone, Jerusalem, Israel), rabbit anti-SK2 (dilution 1:50; APC-028; Alomone) or rabbit anti-SK3 (dilution 1:50; APC-025; Alomone). Slides were then incubated for 2 h in goat anti-rabbit 647 secondary antibody (dilution 1:400; A-21245; Invitrogen, Waltham, MA, USA). All immunohistochemistry steps were performed at room temperature.

RNAscope was performed according to manufacturer's protocols (Wang et al., 2012). ACDBio probes used include tdTomato (317041), SCN8a (434191-C2) and CACNA1d (502591-C2). All slides from both immunohistochemistry and RNAscope were coverslipped using Fluoromount-G with 4′,6-diamidino-2-phenylindole (Invitrogen). Images were acquired as sequential z-stacks of 20× tile-scans on a SP8 confocal microscope (Leica Microsystems). Cell counting was performed manually in ImageJ (NIH, Bethesda, MD, USA) using the multipoint tool. All Shox2 INs in each examined slice were counted. Slices ($n = 7$–12 per animal), at least 200 μm apart, from lumbar segments of the spinal cord were quantified.

## Agglomerative hierarchical clustering

Pearson's linear correlation test was conducted to exclude highly correlated electrophysiological parameters ($P < 0.0001$) from the 18 which are detailed above. Hierarchical cluster analyses were performed on the 11 electrophysiological parameters that were determined to be not highly correlated among each other. These 11 parameters included resting membrane potential, time constant, input capacitance, action potential threshold, sAHP amplitude, PIC area, PIC onset voltage, PIC with descending density, $I_H$ area, $I_T$ density and $I_M$ density. Hierarchical clusters were determined by the correlation distance between pairs of observations and consideration of an average for the distance between clusters. This combination was used because it resulted in the highest cophenetic correlation coefficient (0.3046). The number of clusters was determined considering the cutoff below the maximum inconsistency coefficient for each link. Data were initially standardized to a mean of 0 and a SD of 1 to be able to compare variables with different units in MATLAB (MathWorks Inc., Natick, MA, USA) using customized scripts.

## Modelling methods

The conductance-based single-compartment model of a neuron was developed in the Hodgkin–Huxley style and was based on the previous models (Brocard et al., 2013; Rybak et al., 1997, 2003, 2004). The dynamics of the neuron membrane potential $V$ obeyed the following differential equation:

$$C \cdot \frac{dV}{dt} = -\Sigma\, I_i = -I_{\mathrm{Na}} - I_{\mathrm{NaP}} - I_{\mathrm{K}} - I_{\mathrm{M}} - I_{\mathrm{CaL}} - I_{\mathrm{KCa}} - I_{\mathrm{L}}, \quad (1)$$

where $C$ is the membrane capacitance, $t$ is time and $I_{\mathrm{i}}$ represents different ionic currents. The following conductances were included in the model: fast sodium ($I_{\mathrm{Na}}$), persistent sodium ($I_{\mathrm{NaP}}$), delayed rectifier potassium ($I_{\mathrm{Kdr}}$), M-type potassium ($I_{\mathrm{M}}$), L-type calcium ($I_{\mathrm{CaL}}$), calcium-dependent potassium ($I_{\mathrm{KCa}}$) and leak conductance ($I_{\mathrm{L}}$). These currents were described as follows:

$$I_{\mathrm{Na}} = \bar{g}_{\mathrm{Na}} \cdot m_{\mathrm{Na}}^3 \cdot h_{\mathrm{Na}} \cdot (V - E_{\mathrm{Na}});$$

$$I_{\mathrm{NaP}} = \bar{g}_{\mathrm{NaP}} \cdot m_{\mathrm{NaP}} \cdot h_{\mathrm{NaP}} \cdot (V - E_{\mathrm{Na}});$$

$$I_{\mathrm{K}} = \bar{g}_{\mathrm{K}} \cdot m_{\mathrm{K}}^4 \cdot (V - E_{\mathrm{K}});$$

**Table 1. Steady state activation and inactivation variables and time constants for voltage-dependent conductances.**

| Conductance | $m_\infty(V)$, $h_\infty(V)$, $V$ (in mV); $\tau_m(V)$, $\tau_h(V)$ (in ms) |
|---|---|
| Fast sodium Na | $m_{\infty Na} = 1/(1+\exp(-(V+43.8)/6))$ $\tau_{mNa} = 0$ $h_{\infty Na} = (1+\exp((V+67.5)/10.8))$ $\tau_{hNa} = 35.2/\cosh((V+67.5)/12.8)$ |
| Persistent sodium NaP | $m_{\infty NaP} = 1/(1+\exp(-(V+54.6)/4.2))$ $\tau_{mNaP} = 0$ $h_{\infty NaP} = (1+\exp((V+57)/5))$ $\tau_{hNaP} = T_{hNaP}/\cosh((V+57)/15)$ |
| Delayed rectifier potassium Kdr | $m_{\infty K} = 1/(1+\exp(-(V+34.5)/5))$ $\tau_{hK} = 4/\cosh((V+34.5)/20)$ |
| Potassium M M | $m_{\infty M} = 1/(1+\exp(-(V+44)/4.3))$ $\tau_{hM} = 7/\cosh((V+34.5)/25)$ |
| High- voltage activated calcium, CaL | $m_{\infty CaL} = 1/(1+\exp(-(V+27.4)/5.7))$ $\tau_{mCaL} = 0$ $h_{\infty CaL} = (1+\exp((V+28.5)/6.4))$ $\tau_{hCaL} = 18$ |

$$I_M = \bar{g}_M \cdot m_M \cdot h_M \cdot (V - E_K);$$
$$I_{CaL} = \bar{g}_{CaL} \cdot m_{CaL} \cdot h_{CaL} \cdot (V - E_{Ca});$$
$$I_{KCa} = \bar{g}_{KCa} \cdot m_{KCa}^2 \cdot (V - E_K);$$
$$I_L = g_L \cdot (V - E_L), \quad (2)$$

where $\bar{g}_i$ is the maximal conductance of the channel $i$, $m_i$, and $h_i$ are the activation and inactivation variables of this channel, and $E_i$ is the reversal potential of this channel.

Kinetics of activation and inactivation variables for all voltage-dependent currents are described as follows:

$$\tau_{mi}(V) \cdot \frac{d}{dt} m_i = m_{\infty i}(V) - m_i; \quad (3)$$
$$\tau_{hi}(V) \cdot \frac{d}{dt} h_i = h_{\infty i}(V) - h_i,$$

where $m_{\infty i}$ and $h_{\infty i}$ are steady states for activation and inactivation variables, and $\tau_{mi}$ and $\tau_{hi}$ are the corresponding time constants. The expressions for steady state activation and inactivation variables and time constants for voltage-dependent ionic channels are specified in Table 1.

Activation of $I_{KCa}$ depends on the intracellular calcium concentration, $[Ca^{2+}]_{in}$, and is independent of voltage. The kinetics of $[Ca^{2+}]_{in}$ is modeled according to the following equation:

$$\frac{d}{dt}[Ca^{2+}]_{in} = -\alpha_{Ca} \cdot I_{Ca} + ([Ca^{2+}]_{in0} - [Ca^{2+}]_{in})/\tau_{Ca}, (4)$$

where $\alpha$ characterizes influx of $Ca^{2+}$ ions by $I_{Ca}$ with the account of their buffereng, $\tau_{Ca}$ represents the time constant of $Ca^{2+}$ pump that removes $Ca^{2+}$ and $[Ca^{2+}]_{in0}$ is the base value of intracellular $Ca^{2+}$ concentration. In the present study, $I_{Ca}$ represents $I_{CaL}$.

The following parameters were used for calcium dynamics:

$$\alpha_{Ca} = 5 \cdot 10^{-8}\ \text{mM/fC};\ \tau_{Ca} = 500\ \text{ms},$$
$$\left[Ca^{2+}\right] in^0 = 5 \cdot 10^{-5}\ \text{mM}.$$

Activation of the $Ca^{2+}$-dependent potassium channels, is described by the following equation (Rybak et al., 1997):

$$\tau_{KCa}\left([Ca^{2+}]_{in}\right) \cdot \frac{d}{dt} m_{KCa}\left([Ca^{2+}]_{in}\right) = m_{\infty KCa}\left([Ca^{2+}]_{in}\right) - m_{KCa}\left([Ca^{2+}]_{in}\right), \quad (5)$$

where $m_{\infty KCa}$ and $\tau_{KCa}$ are steady states and time constant for the activation variable:

$$m_{\infty KCa}([Ca^{2+}]_{in}) = \alpha_{KCa} \cdot [Ca^{2+}]_{in}^2/([Ca^{2+}]_{in}^2 + \beta_{KCa}); (6)$$
$$\tau_{KCa}([Ca^{2+}]_{in}) = k_{KCa} \cdot \tau_{KCa0}/([Ca^{2+}]_{in}^2 + \beta_{KCa})$$

The following parameters defining dynamics of these channels were used:

$$\alpha_{KCa} = 1.25 \times 10^{-8};\ \beta_{KCa} = 2.5\text{mM}^2;$$
$$k_{KCa} = 1000\text{mM}^2;\ \tau_{KCa0} = 5\text{ms}.$$

The basic neuronal model parameters were the following:

$$C = 52\ \text{pF};\ E_{Na} = 55\ \text{mV};\ E_K = -80\ \text{mV};$$
$$E_{Ca} = 120\ \text{mV};\ E_L = -62\ \text{mV};\ g_L = 1.7\ \text{nS};$$
$$\bar{g}_{Na} = 220\ \text{nS};\ \bar{g}_K = 150\ \text{nS}.$$

In particular simulations, we varied some maximal conductances:

$$\bar{g}_{NaP} = 0.35 - 1.0\text{nS};\ \bar{g}_M = 0.6 - 2.5\text{nS};$$
$$\bar{g}_{CaL} = 0.25 - 0.5\text{nS};\ \bar{g}_{KCa} = 0.4 - 2.0\text{nS}.$$

Simulations were performed using MATLAB R2023b (MathWorks Inc.). Differential equations were solved using a variable order multistep differential equation solver ode15s available in MATLAB. In each simulation, a settling period of 10–50 s was allowed before data were collected. The scripts to create the simulations presented in the paper are available online (https://github.com/RybakLab/Singh-et-al-2025).

### Statistical analysis

Statistical tests and *post hoc* analyses were performed with Prism (GraphPad Software Inc., San Diego, CA, USA). All results are presented as the mean ± SD, unless otherwise stated. $P < 0.05$ was considered statistically significant. The distribution of the data was determined by the Shapiro–Wilk normality test. In the case of normally distributed data, we performed paired *t* tests to compare baseline and drug conditions or one-way ANOVAs with Tukey's *post hoc* tests to compare three age groups. In the cases where data were not normally distributed, we performed Wilcoxon matched pairs signed ranks tests to compare baseline and drug conditions and Kruskal–Wallis with Dunn's multiple comparisons *post hoc* tests to compare three age groups. Comparisons between age groups of percentages for conductance presence, RNA presence or protein presence were performed with a chi-squared test.

## Results

### Intrinsic passive and active properties of Shox2 INs during development

Spinal Shox2 INs are part of the locomotor CPG that generates rhythmic and patterned motor output across the lifespan (Dougherty et al., 2013). Although mice begin performing regular weight-bearing steps by P9 (Jiang et al., 1999a), many previous studies of locomotor circuitry used neonatal mouse preparations in which locomotor-like activity could be evoked in isolated spinal cords (Anderson et al., 2012; Dougherty et al., 2013; Hinckley et al., 2010). The general neuronal types and connectivity structure in the neonatal spinal cord are hypothesized to be present and similar in function to those in adult mice (Crone et al., 2008, 2009; Danner et al., 2017; Rybak et al., 2015; Talpalar et al., 2013). However, there are some notable differences. Given that strong gap junctional coupling in neonatal locomotor circuits decreases by adulthood (Ha & Dougherty, 2018), we hypothesized that some intrinsic rhythmogenic properties in Shox2 INs increase in magnitude and/or prevalence with age. Such a developmental change may compensate for reduced gap junctional coupling and maintain locomotor rhythm in adults. To compare properties of these neurons at neonatal, adult and an intermediate juvenile stage, we first examined the basic electrophysiological properties of Shox2 INs across postnatal maturation. We recorded passive and active properties using whole cell patch clamp in lumbar spinal slices targeting 35 neonatal (P2–5, mean age 3.2 ± 0.980 postnatal days), 33 juvenile (P14–21, mean age 17.2 ± 1.61 postnatal days) and 36 adult (P60+, mean age 96.2 ± 28.52 postnatal days) fluorescently labelled Shox2 INs (Table 2). We found that neonatal Shox2 INs have a more depolarized action potential threshold voltage (−30.5 ± 4.3 mV, $n = 35$) compared to adult Shox2 INs (−33.2 ± 4.7 mV, $n = 36$; one-way ANOVA with Tukey's *post hoc* test, $P = 0.0279$). Neonatal Shox2 INs have a longer time constant (53.0 ± 29.5 ms, $n = 35$) compared to juvenile (33.4 ± 12.4 ms, $n = 33$; Kruskal–Wallis with Dunn's *post hoc* test, $P = 0.0021$) and adult (31.2 ± 17.0 ms, $n = 36$; Kruskal-Wallis with Dunn's *post hoc* test, $P < 0.0001$) Shox2 INs. We also report a higher input capacitance in neonatal Shox2 INs (54.3 ± 17.3 pF, $n = 35$) compared to juvenile (47.1 ± 25.3 pF, $n = 32$; one-way ANOVA with Tukey's *post hoc* test, $P = 0.0149$) and adult (43.1 ± 16.8 pF, $n = 36$; one-way ANOVA with Tukey's *post hoc* test, $P = 0.0104$) Shox2 INs, which is consistent with the findings reported for lumbar spinal V2a INs (Husch et al., 2015). We found no significant differences between the age groups in resting membrane potential, input resistance, rheobase and leak conductance. These findings indicate relatively modest differences in active and passive electrophysiological properties in lumbar spinal Shox2 INs across postnatal age which are consistent with previously reported developmental changes in lumbar spinal INs (Borowska et al., 2015, Husch et al., 2015).

### The hyperpolarization-activated, T-type calcium and A-type potassium currents are found in subsets of Shox2 INs across postnatal age

To reveal the extent to which Shox2 INs display voltage-sensitive rhythmogenic properties across postnatal development, we recorded voltage-sensitive conductances that have been previously shown to shape bursting and firing properties in other neuron types (Harris-Warrick, 2010). This included $I_{\mathrm{H}}$ (Fig. 1*A*,*B*), which was present in approximately half of the recorded neonate ($n = 20/53$; 57%) and adult ($n = 18/36$; 50%) Shox2 INs, and a slightly larger subset of juvenile ($n = 21/32$; 66%) Shox2 INs (Fig. 1*C*). The current density of $I_{\mathrm{H}}$ did not change across postnatal age groups (Fig. 1*D*). We also recorded $I_{\mathrm{T}}$ (Fig. 1*E*,*F*) and $I_{\mathrm{A}}$ (Fig. 1*I*,*J*) in subsets of Shox2 INs across postnatal development. Both $I_{\mathrm{T}}$ (Fig. 1*G*) and $I_{\mathrm{A}}$ (Fig. 1*H*) were present in ≤17% of Shox2 INs across all three age groups. The current density of $I_{\mathrm{T}}$ does increase from neonate (0.44 ± 0.23 pA pF$^{-1}$, $n = 6$) to adult (1.13 ± 0.50 pA pF$^{-1}$, $n = 10$; one-way ANOVA with Tukey's *post hoc* test, $P = 0.0179$) Shox2 INs, despite being a rarely displayed property in these neurons (Fig. 1*H*). The current density of $I_{\mathrm{A}}$ did not change across postnatal age groups ($n = 12$) (Fig. 1*L*). The *I–V* curves for each of these three conductances in Shox2 INs matches what has been previously shown in other neurons (Anderson et al., 2012; Huguenard et al., 1991; Rivera-Arconada et al., 2013). These findings reveal that all three tested conductances occur in subsets of Shox2 INs from all age groups.

## Shox2 INs display PICs which increase in magnitude with age, and express RNA for PIC-related ion channels

To record the presence of persistent depolarizing conductances, we used voltage ramps to isolate PICs in Shox2 INs (Fig. 2*A*, *B*). We found that most neonatal ($n = 27/35$; 77%), juvenile ($n = 29/32$; 91%) and adult ($n = 31/36$; 86%) Shox2 INs display a PIC in response to slow current ramp (Fig. 2*C*). In addition to PICs being present on the ascending phase of the voltage ramp, we found that a small subset of Shox2 INs display PICs on both the ascending and descending phases of the ramp (Fig. 2*D*). In these cases, the current onset occurs on the ascending phase of the ramp, whereas the offset occurs on the descending phase (Fig. 2*B*). The PIC continued into the descending phase of the ramp in a small subset of PICs in juvenile ($n = 6/32$; 19%) and adult ($n = 6/36$; 17%) but this feature was largely missing from neonatal ($n = 1/35$; 3%) Shox2 INs (Fig. 2*D*). The presence of PICs on the descending phase of the voltage ramp may be a

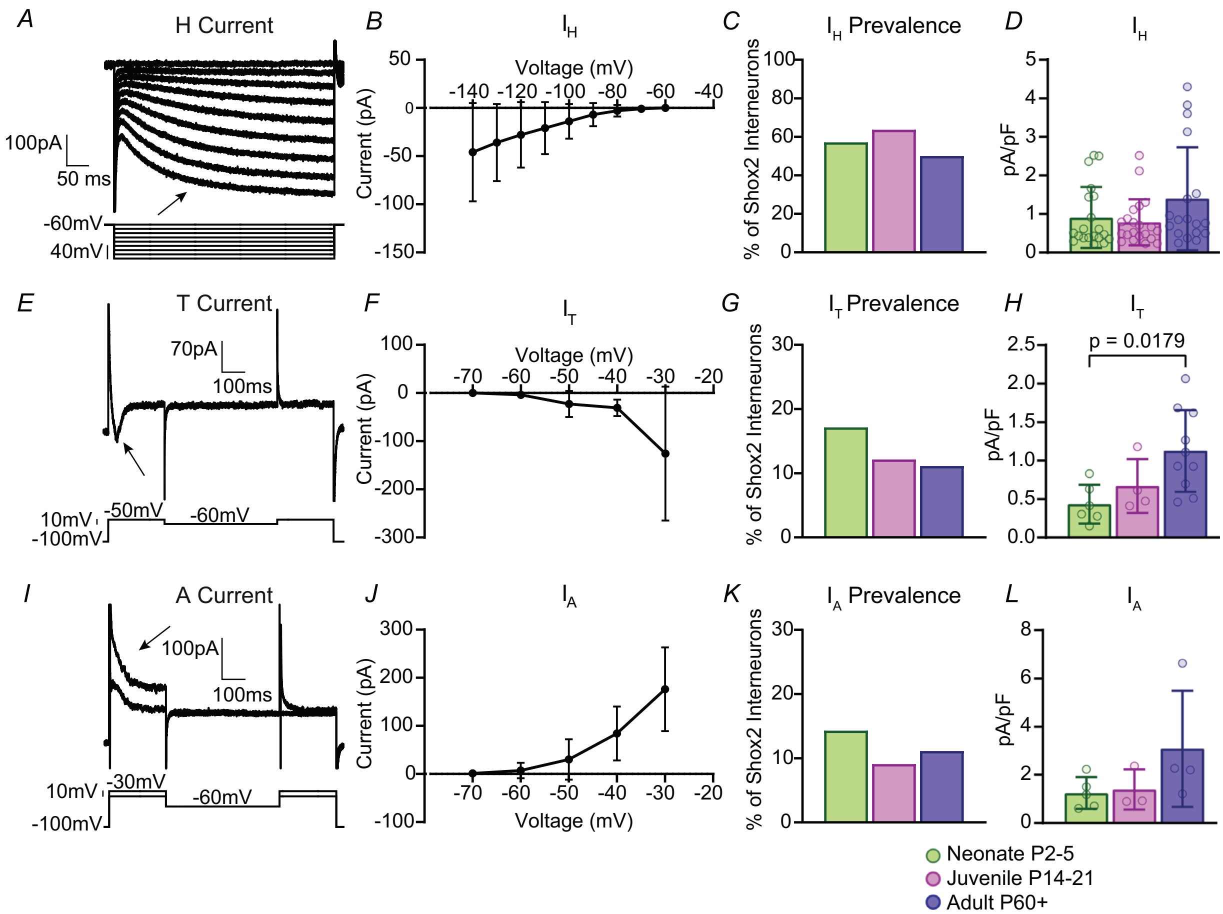


**Figure 1. $I_H$, $I_T$ and $I_A$ are found in subsets of Shox2 INs**
*A*, inward current responses to hyperpolarizing voltage steps from –60 mV. Arrow indicates the presence of $I_H$ in an example from an adult Shox2 IN. *B*, *I–V* curve of $I_H$ from all Shox2 INs with $I_H$ ($n = 59$). *C*, 50–66% of Shox2 INs display $I_H$. *D*, $I_H$ current densities are relatively consistent through postnatal development. Error bars indicate SD. *E*, inward current response to depolarizing voltage step from –100 mV, and not from –60 mV. Arrow indicates the presence of $I_T$ an example from an adult Shox2 IN. *F*, *I–V* curve of $I_T$ from all Shox2 INs with $I_T$ ($n = 20$). *G*, <18% of Shox2 INs display $I_T$. *H*, $I_T$ current density increases from neonate to adult. One-way ANOVA with Tukey's *post hoc* test. Error bars indicate SD. *I*, outward current response to depolarizing voltage step from –100 mV, and not from –60 mV. Arrow indicates the presence of $I_A$ in an example from an adult Shox2 IN. *J*, *I–V* curve of $I_A$ from all Shox2 INs with $I_A$ ($n = 12$). *K*, <15% of Shox2 INs display $I_A$. *L*, $I_A$ current densities do not change significantly with age. Error bars indicate the SD. [Colour figure can be viewed at wileyonlinelibrary.com]

**Table 2. Comparison of intrinsic passive and active properties in Shox2 interneurons from three age groups.**

| | Neonate P2–5 (mean ± SD) | Juvenile P14–21 (mean ± SD) | Adult P60+ (mean ± SD) | One-way ANOVA or Kruskal–Wallis *H* test | *P* |
|---|---|---|---|---|---|
| Membrane potential (mV) | −45.6 ± 4.1 | −46.1 ± 4.5 | −48.0 ± 4.3 | $F_{2,101}$ = 2.998 | 0.0534 |
| Input resistance (MΩ) | 1077.0 ± 685.3 | 813.2 ± 484.5 | 792.7 ± 458.2 | H(2) = 5.437 | 0.066 |
| Capacitance (pF) | 54.3 ± 17.3 | 47.1 ± 25.3 | 43.1 ± 16.8 | $F_{2,100}$ = 5.658 | 0.0047* |
| Leak (nS) | 1.3 ± 0.9 | 1.5 ± 0.7 | 1.7 ± 1.1 | $F_{2,101}$ = 1.798 | 0.171 |
| Time constant (ms) | 53.0 ± 29.5 | 33.4 ± 12.4 | 31.2 ± 17.0 | $H_2$ = 20.24 | <0.0001* |
| Rheobase (mV) | 21.3 ± 15.6 | 21.9 ± 11.1 | 22.1 ± 20.6 | $F_{2,101}$ = 0.0202 | 0.98 |
| Threshold (mV) | −30.5 ± 4.3 | −32.6 ± 4.0 | −33.2 ± 4.7 | $F_{2,101}$ = 3.657 | 0.0293* |

* $P < 0.05$.

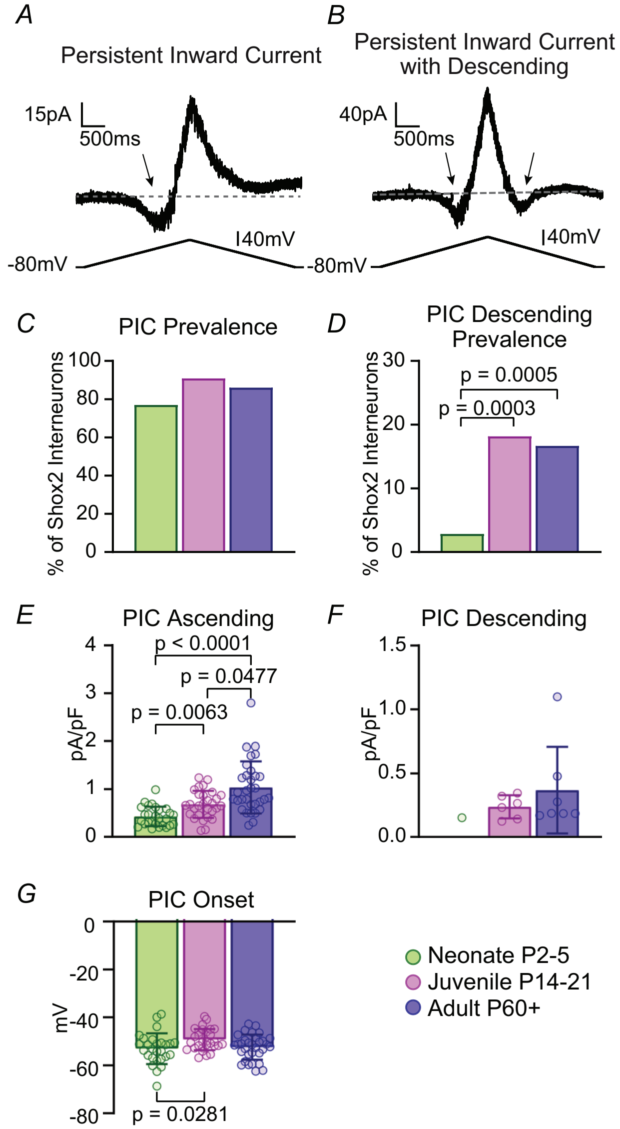


**Figure 2. Subsets of Shox2 INs display PICs which increase in magnitude with age**

*A* and *B*, examples of inward currents in adult Shox2 INs in response to slow voltage ramps from –80 mV to –10 mV, and back to -80 mV. Arrows indicate the presence of PICs, some of which are only present in the first part of the ramp (*A*) and others persist in the descending phase of the ramp (*B*). *C*, PICs are present in most (<75%) Shox2 INs from all age groups. *D*, PICs continuing into the descending phase of the ramp are less prevalent (<20%) in juvenile and adult Shox2 INs, and are even less prevalent in neonate Shox2 INs (3%) compared to juvenile (chi-squared, degrees of freedom = 2, *P* = 0.0003) or adult (chi-squared, degrees of freedom = 2, *P* = 0.0005). *E*, PICs increase in current density from neonate (green) to juvenile (pink) to adult (purple) Shox2 INs. *F*, current densities of the relatively few Shox2 INs which display PIC with descending. Kruskal–Wallis with Dunn's *post hoc* test. Error bars indicate SD. *G*, mean onset of PICs in response to the ascending voltage ramp is more depolarized in juvenile compared to neonateShox2 INs. One-way ANOVA with Tukey's *post hoc* test. Error bars indicate the SD. [Colour figure can be viewed at wileyonlinelibrary.com] result of either the strength of the PIC that carries over the duration of the voltage ramp, the time constant of the slow inactivation of PICs or a shifted voltage dependence of deinactivation in the subset of Shox2 INs displaying the descending PICs.

Because PICs can be mediated by both sodium and calcium components, we further examined the voltage properties and pharmacological sensitivities of PICs in Shox2 INs across postnatal development. The current density of PICs on the ascending phase of the voltage ramp increases from neonate ($0.42 \pm 0.20$ pA pF$^{-1}$, $n = 27$) to juvenile ($0.68 \pm 0.28$ pA pF$^{-1}$, $n = 29$; Kruskal–Wallis test with Dunn's *post hoc* test, $P = 0.0063$) and juvenile to adult ($1.03 \pm 0.54$ pA pF$^{-1}$, $n = 31$; Kruskal–Wallis test with Dunn's *post hoc* test, $P = 0.0477$) (Fig. 2*E*). Because PICs persisting onto the descending phase of the voltage ramp were rarely present, particularly in neonates (Fig. 2*D*), we were unable to test for a statistical change in its magnitude with development (Fig. 2*F*). We found that PIC onset is more depolarized in juvenile ($-49 \pm 4.5$ mV, $n = 29$) compared to neonatal Shox2 INs ($-53 \pm 6.3$ mV, $n = 27$; one-way ANOVA with Tukey's *post hoc* test, $P = 0.0281$), which are similar to the adult Shox2 INs ($-52 \pm 5.2$ mV, $n = 31$) (Fig. 2*G*). These data demonstrate that there are developmental increases in PIC magnitude in Shox2 INs. We then considered whether PICs in adult Shox2 INs consist of persistent sodium ($I_{NaP}$) and L-type calcium ($I_{CaL}$) components. We applied 10 μM riluzole (Fig. 3*A*) or 20 μM nimodipine (Fig. 3*B*) to block these currents respectively in adult Shox2 INs, using an intracellular solution containing cesium to increase space clamp. With the inclusion of cesium, all ($n = 20/20$) Shox2 INs displayed PICs on both the ascending and the descending phases of the voltage ramp. Riluzole ($n = 12$) and nimodipine ($n = 8$) application resulted in a mean decrease of 34% and 14% in current amplitude, respectively (Fig. 3*C*, *D*). However, only riluzole application resulted in a decreased PIC on the descending phase of the ramp (Fig. 3*C*, right).

Having observed both sodium and calcium components of PICs, we next investigated whether lumbar spinal Shox2 INs display channels correlated to these conductances. We examined four postnatal ages: 2, 7, 14 and 64 days. We began with $Na_V1.6$, a voltage-gated sodium channel responsible for mediating $I_{NaP}$ in other neuron populations (Katz et al., 2018; Sharples & Miles, 2021). Using immunohistochemistry, we were unable to visualize $Na_V1.6$ expression colocalized to tdTomato positive Shox2 Ins, which is probably a result of predominant expression patterns in the axon initial segments of neurons (Drouillas et al., 2023). Visualization of Shox2 IN axon initial segments is difficult because of their mixed orientations and a lack of tdTomato expression in cellular compartments beyond the soma. Therefore, we performed RNAscope *in situ* hybridization to visualize RNA within lumbar spinal Shox2 IN cell bodies at four ages. With this method, we found that $Na_V1.6$ RNA is highly prevalent in Shox2 INs at all ages examined (Fig. 3*E*). We next targeted $Ca_V1.3$, a voltage-gated calcium channel which mediates $I_{CaL}$ (Jiang, et al., 1999b). $Ca_V1.3$ RNA is present in a large proportion (<67%) of examined lumbar spinal Shox2 INs at 2, 7, 14 and 64 postnatal days (Fig. 3*F*).

Together, these data show that Shox2 INs display sodium- and calcium-mediated PICs that increase in amplitude with age, as well as RNA transcripts for channels that can mediate $I_{NaP}$ and $I_{CaL}$ components of PICs.

## Shox2 INs display M currents which increase in magnitude with age and express voltage-gated potassium channels

$I_M$ (Fig. 4*A*) is the most prevalent current in Shox2 INs among all examined ionic currents and across all three age groups (Fig. 4*B*). We found that most neonatal ($n = 31/35$; 87%), juvenile ($n = 28/32$; 88%) and adult ($n = 31/36$; 86%) Shox2 INs display the tail relaxation curve from $I_M$ (Fig. 4*B*). We hypothesized that this property increases in magnitude with age. We found that $I_M$ does increase in magnitude between neonate ($1.17 \pm 0.44$ pA pF$^{-1}$, $n = 31$) and adult ($2.26 \pm 1.7$ pA pF$^{-1}$, $n = 31$; Kruskal–Wallis test with Dunn's *post hoc* test, $P = 0.0173$) (Fig. 4*C*) Shox2 INs, with juvenile $I_M$ magnitude residing between ($1.78 \pm 1.08$, $n = 28$). $I_M$ is mediated by heteromers of two voltage-gated potassium channel subunits: $K_V7.2$ and $K_V7.3$ (Wang et al., 1998). We blocked $K_V7.2/3$ channels by applying XE991 (Greene et al., 2017) and measured a mean 51% decrease in $I_M$ amplitude, confirming that this current is mediated by $K_V7.2/3$ channels in Shox2 INs (mean age $4.25 \pm 3.03$ postnatal days) (Fig. 4*D*). We visualized these channels in lumbar spinal Shox2 INs across postnatal development using immunohistochemistry and found that Shox2 INs express both channel subunits at all ages examined (Fig. 4*E* and *F*). These data show that $K_V7.2/3$-mediated $I_M$ increases in magnitude across postnatal development in Shox2 INs, and that Shox2 INs express $K_V7.2/3$ channels from neonatal ages through adulthood.

## Juvenile and adult Shox2 INs display sAHP and express calcium-dependent potassium channels

We observed biphasic AHPs, indicative of sAHP, in current clamp (Fig. 5*A*) in a subset of juvenile ($n = 18/32$; 56%) and adult ($n = 20/36$; 56%) Shox2 INs, and rarely in neonatal INs ($n = 1/35$; 3%) (Fig. 5*B*). The amplitude (Fig. 5*C*) and duration (Fig. 5*D*) of the sAHP was similar between juvenile and adult Shox2 INs. We also found that the sAHP in Shox2 INs is sensitive to apamin (Fig. 5*E*), a blocker for SK2 and SK3 calcium-dependent potassium channels (Köhler et al., 1996), because it completely eliminated the sAHP in all but one tested adult Shox2 IN ($n$ = 9/10) (Fig. 5*F*, *G*). As sAHP increases in prevalence at juvenile and adult stages, we hypothesized that the channels mediating it would also increase in prevalence with age in Shox2 INs. Motor neurons have been shown to display an apamin-sensitive sAHP mediated by the calcium-dependent potassium channels SK2 and SK3 (Deardorff et al., 2013), and so we examined these channels in Shox2 INs using immunohistochemistry. We found that SK2 (Fig. 5*H*) and SK3 (Fig. 5*I*) channels are rarely present in examined Shox2 INs from the youngest ages studied here, P2 (2–17%) and P7 (5–16%). However,

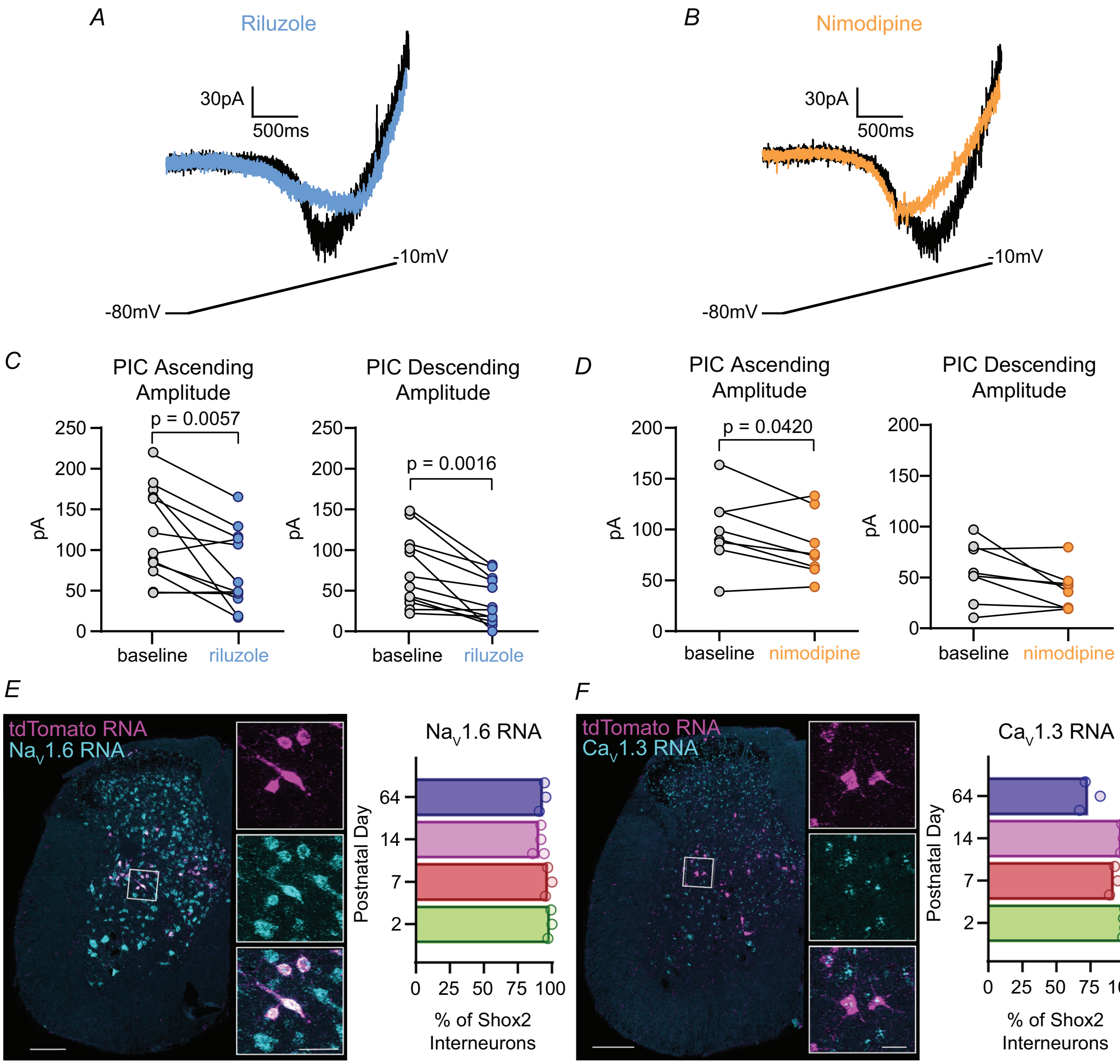


**Figure 3. Subsets of Shox2 INs display PICs which have both sodium and calcium components**
*A*, representative examples of PICs from an adult Shox2 IN at baseline (black) and following riluzole application (blue). *B*, representative examples of PICs from an adult Shox2 IN at baseline (black) and following nimodipine application (orange). *C*, riluzole decreases the amplitudes of PICs measured in both the ascending and descending phases of the ramp, paired *t* test. *D*, nimodipine decreases the amplitudes of PICs but not the descending phase of PICs, paired *t* test. *E*, representative images of RNA for Na$_V$1.6 (cyan) and tdTomato (magenta) in the lumbar spinal slice. >85% of tdTomato RNA-containing cells also contain NA$_V$1.6 RNA across all four ages examined. *F*, representative images of RNA for Ca$_V$1.3 (cyan) and tdTomato (magenta) in the lumbar spinal slice. Lumbar spinal sections have tdTomato RNA-containing cells that also contain Ca$_V$1.3 RNA at all three ages examined. Scale bars for spinal sections = 200 µm, insets = 25 µm. [Colour figure can be viewed at wileyonlinelibrary.com]

30% of juvenile (P14) and adult (P64) Shox2 INs express SK2 channels and 31% express SK3 channels (Fig. 5*H* and *I*). These SK channels have robust expression in other spinal neuron types as well. Taken together, we show that sAHP magnitude and SK2/3 channel expression are similarly increased in Shox2 INs at juvenile and adult time points.

## Unbiased hierarchical clustering reveals age-specific groups of Shox2 INs based on electrophysiological properties

The numerous electrophysiological properties measured in Shox2 INs may shape their recruitment and ability to fire action potentials and/or bursts. To compare sub-groupings of electrophysiologically identified Shox2 INs and possibly reveal additional age-dependent differences amongst this heterogeneous population, we next considered all 104 Shox2 neurons, spanning the three age groups, with properties measured in both current clamp and voltage clamp. We performed hierarchical cluster analysis (Garcia-Ramirez et al., 2022) using the 11 electrophysiological measurements recorded from these neurons that were not highly correlated amongst themselves. This produced eight clusters, portrayed in the dendrogram where each leaf (individual Shox2 IN) is shaded accordingly (Fig. 6*A*). The distribution of clusters within the three age groups showed that neonatal

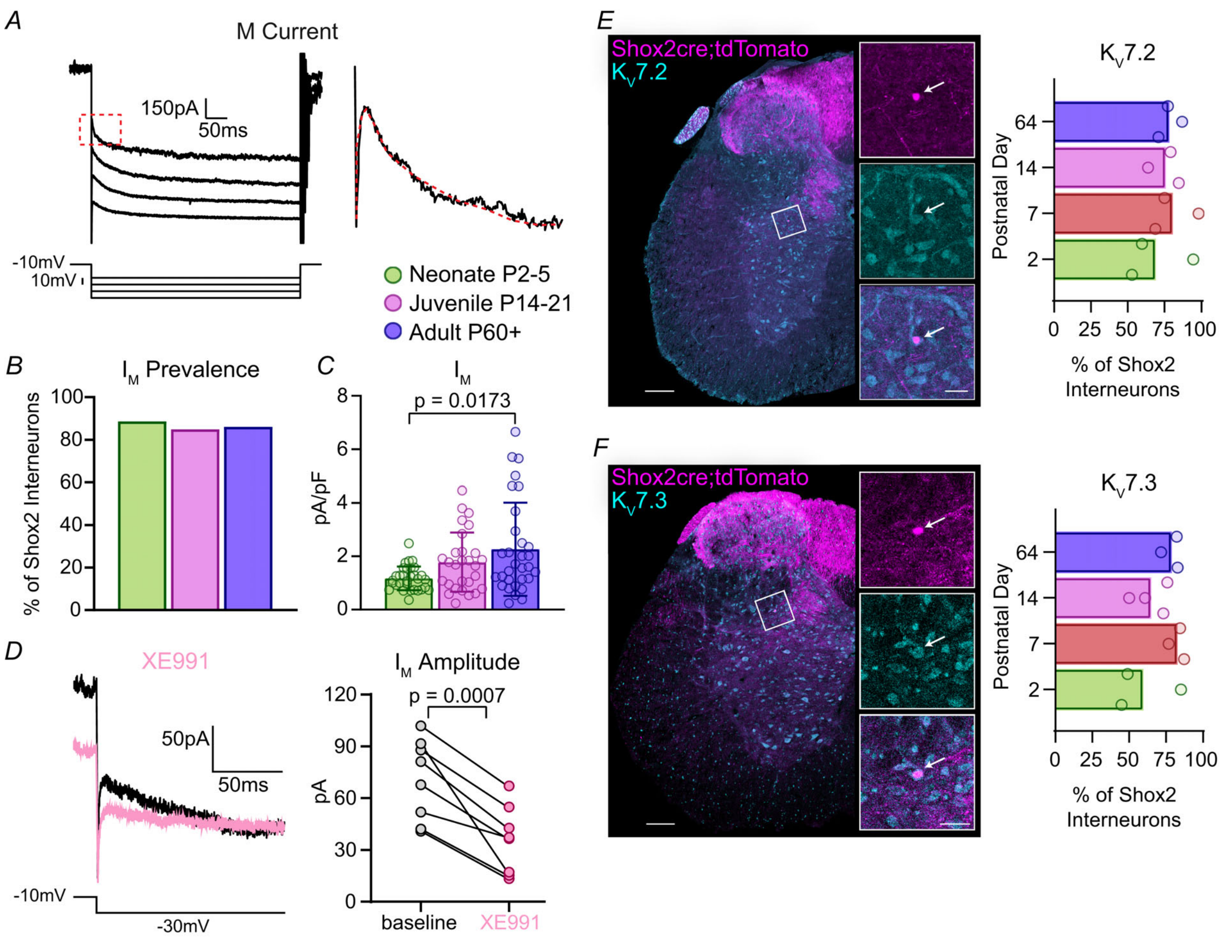


**Figure 4. Subsets of Shox2 INs display M currents which increase in magnitude with age and express $K_V$7.2/3 subunits**

*A*, outward current responses to hyperpolarizing voltage steps from −10 mV in an example from an adult Shox2 IN. Red dotted box and line highlight tail relaxation curve of of $I_M$. *B*, $I_M$ is the most prevalent property (≥85%) in Shox2 INs across all age groups among those examined in this study. *C*, $I_M$ current density increases from neonate (green) to adult (purple). Kruskal–Wallis with Dunn's *post hoc* test. Error bars indicate the SD. *D*, Representative $I_M$ tails from baseline (black) and XE991 (pink) conditions an example from a neonatal Shox2 IN. XE991 decreases the amplitude of $I_M$ tails. Paired *t* test. *E* and *F*, representative images and quantification of (*E*) $K_V$7.2 and (*F*) $K_V$7.3 expression using immunohistochemistry. Channel expression is cyan and tdTomato expression signifying Shox2 is magenta. ≥50% of tdTomato$^+$ neurons express $K_V$7.2 or $K_V$7.3 across all ages examined. Scale bars for spinal sections = 200 μm, insets = 25 μm. [Colour figure can be viewed at wileyonlinelibrary.com]

Shox2 INs consisted only of three electrophysiological subtypes, clusters 1 (54%), 2 (29%) and 3 (17%), whereas juvenile and adult Shox2 INs consisted of seven subtypes, clusters 2–8 (Fig. 6*B*). Cluster numbers were ordered based on their prevalence in age-related groupings. The first three clusters, which are the only groups containing neonatal Shox2 INs, did not have a sAHP (Fig. 6*E*). Clusters 4–8, composed of only juvenile and adult cells, are characterized by similarities to cluster 3 other than the presence of sAHP (cluster 4), the presence of PICs with descending components and high input capacitance (cluster 5) (Fig. 6*C*), hyperpolarized resting membrane potential (cluster 6), an increased $I_M$ density (cluster 7) (Fig. 6*D*) and an increased $I_T$ density (cluster 8). These findings are aligned with what we have shown in Figures 2–5 by comparing these properties between the three age groups. The clustering reveals that the greatest developmental shift in the electrophysiological properties

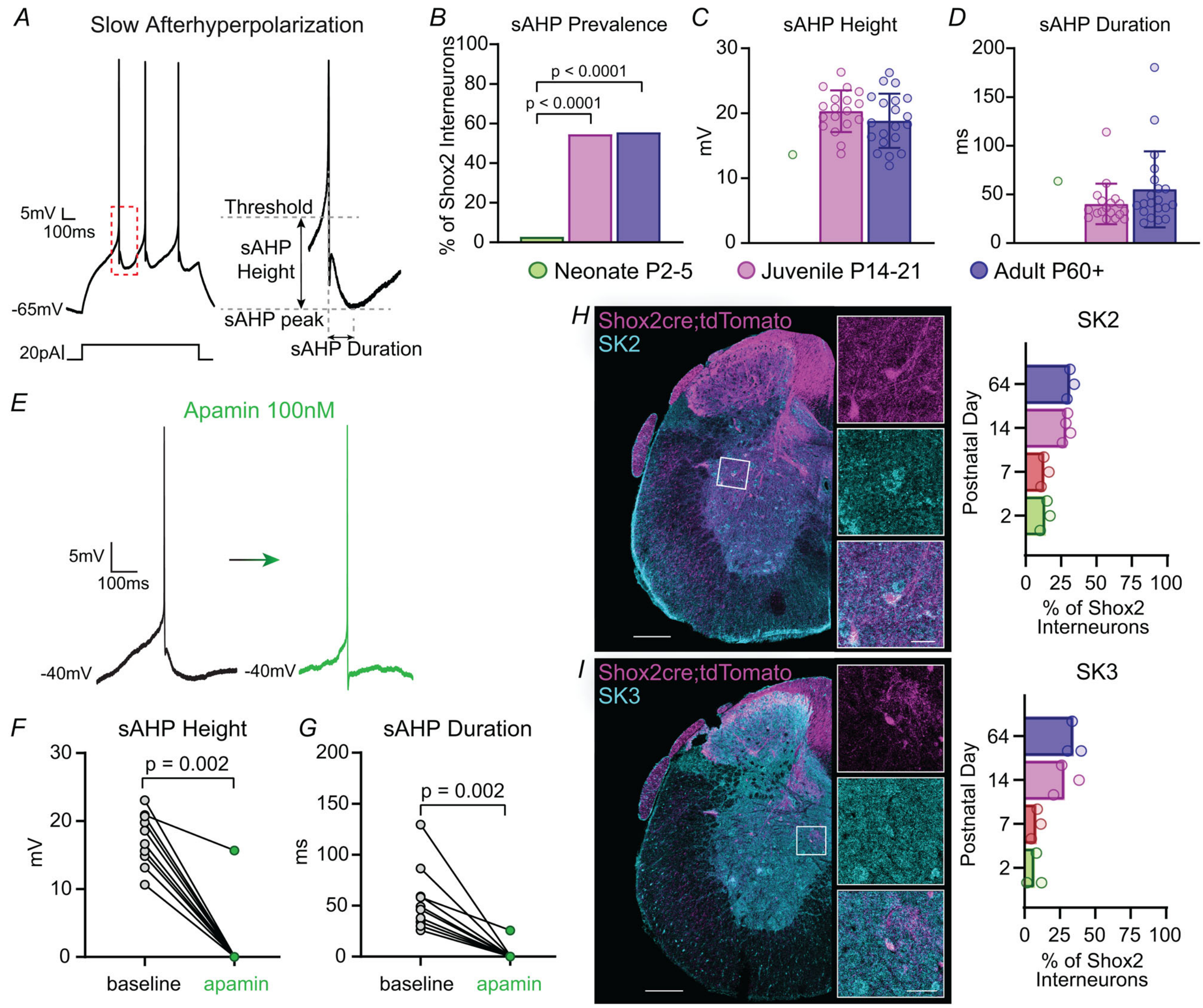


**Figure 5. Subsets of juvenile and adult Shox2 INs display sAHP and express SK2 and SK3**
*A*, representative example of action potentials with sAHP in an adult Shox2 IN in response to depolarizing current step. Red dotted box indicates inset highlighting the sAHP, with height and duration measured as shown. *B*, sAHP is rare in neonate Shox2 INs compared to juvenile (chi-squared, degrees of freedom = 2, $P < 0.0001$) or adult (chi-squared, degrees of freedom = 2, $P < 0.0001$). *C*, comparison of sAHP height and (*D*) duration, which is consistent between juvenile and adult stages. Error bars indicate the SD. *E*, example of an action potential at baseline with a sAHP (black), and following application of apamin, which blocks the sAHP (green). *F*, apamin decreases both the sAHP height and (*G*) duration. Paired *t* test. *H*, representative images and quantification of SK2 and (*I*) SK3 expression using immunohistochemistry. Channel expression is in cyan and tdTomato expression signifying Shox2 is in magenta. SK2 and SK3 expression is lower in neonatal (P2 and P7) Shox2 INs compared to juvenile (P14) and adult (P64). Scale bars for spinal sections = 200 μm, insets = 25 μm. [Colour figure can be viewed at wileyonlinelibrary.com]

of Shox2 INs occurs following the neonatal stage, leading both juvenile and adult Shox2 INs to be relatively more heterogenous in their electrophysiology.

## Computational models of single Shox2 INs simulate voltage clamp protocols and neuronal bursting

A single-compartment, conductance-based (Hodgkin-Huxley style) computational model of a single Shox2 IN was developed to simulate neuronal behaviour in the experimental protocols used in this study. The model included the following ionic currents: fast sodium ($I_{Na}$), persistent sodium ($I_{NaP}$), delayed rectifier potassium ($I_{Kdr}$), M-type potassium ($I_M$), high-voltage activated potassium ($I_{CaL}$), calcium-dependent potassium ($I_{KCa}$) and leak conductance ($I_L$).

The populations of Shox2 INs represented in these single-cell models represent five groups of Shox2 INs derived from the clusters which were generated based on electrophysiological measurements. From the eight clusters (Fig. 6*A*), we considered electrophysiological similarities and age to condense to five groups of Shox2 INs, each representing a single neuron computational model (Fig. 7*A*). The properties of Group I are those of Shox2 INs from cluster 3, defined by relatively low amplitude PICs. Group II represents neonatal cluster 1, defined by relatively higher amplitude PICs. Group III is a combination of clusters 4, 6 and 8, which are juvenile and adult Shox2 INs defined by relatively low amplitude PICs and low amplitude $I_M$. Group IV is adult Shox2 INs from cluster 7 defined by relatively low amplitude PICs and high amplitude $I_M$. Group V is adult Shox2 INs from cluster 5, defined by relatively high amplitude PICs and low amplitude $I_M$. Of note, only groups III–V, which represent adult Shox2 INs, possess $I_{KCa}$ because this conductance is not found in neonatal Shox2 INs (Fig. 6*E*). Cluster 2 was not considered in the generation of these single neuron models because it is comprised of Shox2 INs that contain very little or no PIC.

The maximal conductances $\bar{g}_{NaP}$, $\bar{g}_{CaL}$ and $\bar{g}_M$ for each group were calculated from the averaged experimentally measured maximal values of these currents ($I_{imax}$), the

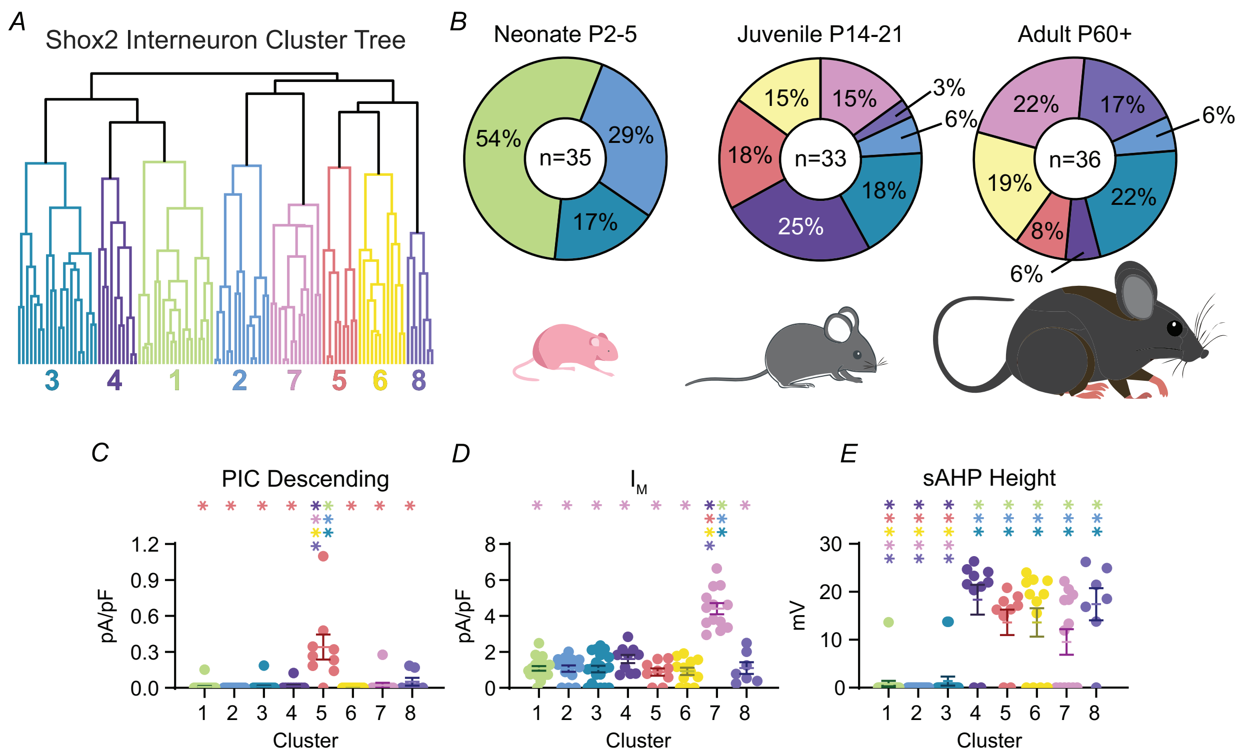


**Figure 6. Unbiased hierarchical clustering of Shox2 INs**
*A*, dendrogram including 104 Shox2 INs, clustered according to 11 electrophysiological properties: resting membrane potential, time constant, input capacitance, threshold, sAHP height, PIC and $I_H$ areas under the curve, PIC onset voltage and current densities for PIC descending, $I_T$ and $I_A$. *B*, neonatal Shox2 INs are comprised of cluster 1 and subsets of clusters 2 and 3. Juvenile and adult Shox2 INs are comprised of subsets of clusters 2–8. *C*, comparisons of current density of PIC descending, (*D*) $I_M$ and (*E*) sAHP height between clusters, where cluster 1 has the highest percentage of neonatal Shox2 INs, and cluster 8 has the highest percentage of adult Shox2 INs. *$P < 0.05$, one-way ANOVA with Tukey's *post hoc* test or Kruskal–Wallis with Dunn's *post hoc* test. Error bars indicate the SD. *Significantly different from the corresponding colour-coded group. [Colour figure can be viewed at wileyonlinelibrary.com]

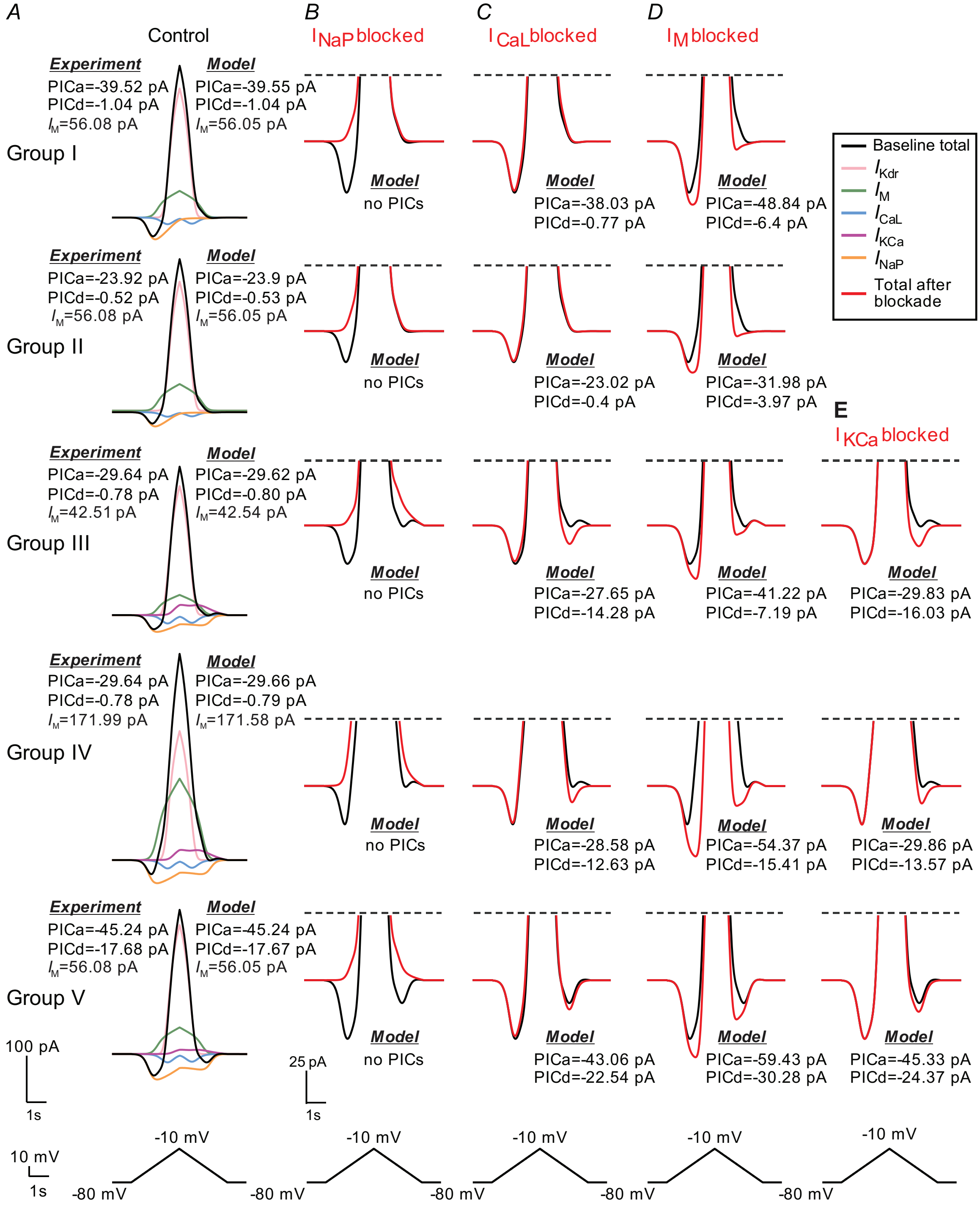


**Figure 7. Simulations of voltage ramp experiments at baseline and following blockade of individual conductances in single neuron model**

*A*, voltage ramp simulations for groups I–V based on experimental data from Shox2 INs. Individually, $I_{Kdr}$ (pink), $I_M$ (green), $I_{CaL}$ (blue), $I_{KCa}$ (purple) and $I_{NaP}$ (gold) contribute to the total PIC (black) in each group. PICa, PIC on the ascending phase of the ramp. PICd, PIC on the descending phase of the ramp. *B*, blockade of $I_{NaP}$ in groups I–V. *C*, blockade of $I_{CaL}$ in groups I–V. *D*, blockade of $I_M$ in groups I–V. *E*, blockade of $I_{KCa}$ in groups III–V. The following model parameters were used: for group I, $\bar{g}_{NaP} =$ 0.6 nS, $\bar{g}_{CaL}$ = 0.4 nS, $\bar{g}_M$ = 0.8 nS; for group II, $\bar{g}_{NaP}$ = 0.39 nS, $\bar{g}_{CaL}$ = 0.27 nS, $\bar{g}_M$ = 0.8 nS; for group III, $\bar{g}_{NaP}$ = 0.4 nS, $\bar{g}_{CaL}$ = 0.5 nS, $\bar{g}_M$ = 0.6 nS; $\bar{g}_{KCa}$ = 0.95 nS; for group IV, $\bar{g}_{NaP}$ = 0.55 nS, $\bar{g}_{CaL}$ = 0.5 nS, $\bar{g}_M$ = 2.45 nS, $\bar{g}_{KCa}$ = 0.95 nS; and for Group V, $\bar{g}_{NaP}$ = 0.55 nS, $\bar{g}_{CaL}$ = 0.5 nS, $\bar{g}_M$ = 0.8 nS; $\bar{g}_{KCa}$ = 0.4 nS. Maximal time constant for $I_{NaP}$ inactivation ($T_{hNaP}$) was set to 3.1 s for neonatal groups I and II and 22 s adult groups III–V. [Colour figure can be viewed at wileyonlinelibrary.com] corresponding voltage value at which the current reaches its maximum ($V_{imax}$) and the descriptions of these currents in the model (see Methods).

$$g_i = \frac{I_{i\ max}}{(V_{i\ max} - E_i)} = \bar{g}_i \cdot m_i\,(V_{i\ max}) \cdot h_i\,(V_{i\ max})\,. \quad (7)$$

Therefore:

$$\bar{g}_i = \frac{g_i}{m_i\,(V_{i\ max}) \cdot h_i\,(V_{i\ max})}. \quad (8)$$

Because PICs in Shox2 INs can include both sodium and calcium components (Fig. 3*A* and *B*) we considered the experimental PICs as compositions of these two currents. An estimation of maximal conductances of these two currents was made after application of the corresponding blockers.

We simulated voltage ramp experiments for groups I–V (Fig. 7*A*), where coloured lines indicate individual current contributions to the resultant PIC in black. Our models correspond tightly to experimental data values. We also simulated the effect of the application of blockers of individual conductances on the total PIC (Fig. 7*B–E*). Blockade of $I_{NaP}$ (Fig. 7*B*) eliminated PICs on both the ascending and descending phases of the voltage ramp in all groups. Blockade of $I_{CaL}$ (Fig. 7*C*) in groups I and II did not have much effect on PICs. However, in groups III–V, $I_{CaL}$ blockade had little effect of ascending PICs and increased PICs on the descending phase of the voltage ramp. Blockade of $I_M$ (Fig. 7*D*) resulted in an increased PIC in all groups, and blockade of $I_{KCa}$ (Fig. 7*E*) did not affect the ascending PICs but it increased the descending PIC in groups III–V. These results suggest a strong interplay of the conductances measured from Shox2 INs across postnatal development.

Our experimental data did not include Shox2 INs which displayed intrinsic rhythmic firing behaviour. This could be because the recorded neurons lacked sufficiently high maximal conductances of $I_{NaP}$ to intrinsically burst, even in the case of adult Shox2 INs in groups III–V ($\bar{g}_{NaP} <$ 0.6 nS). Therefore, we used our model to simulate and predict the effect of increasing $\bar{g}_{NaP}$. We show that an increase of $\bar{g}_{NaP}$ to 1.0 nS allows the simulated cell to generated intrinsic bursting in some range of neuronal excitability (Fig. 8*A*). We confirmed this experimentally in adult Shox2 INs by applying veratridine to enhance $I_{NaP}$ (Fig. 8*B*), which converted tonic firing into rhythmic bursting activity ($n$ = 3). These data from modelling and experimentation suggests that adult Shox2 INs with realistic electrophysiological properties could be capable of $I_{NaP}$-driven rhythmic bursting behaviour.

## Discussion

We investigated the changes in electrophysiological profiles and underlying channel expression within rhythm generating neurons in the lumbar spinal cord during postnatal development. Our results show that subsets of lumbar spinal Shox2 INs display numerous voltage-dependent conductances and their respective channels or RNA transcripts from neonates, juveniles capable of weight-supported stepping and adult mice. We show that currents linked to neuronal bursting, including PIC, $I_M$ and sAHP, increase in prevalence and/or magnitude in Shox2 INs as the mouse develops. Furthermore, the diversity of electrophysiologically-defined subtypes of Shox2 INs increases with age, and subtypes of mature Shox2 INs are distinguished by the expression of voltage-gated conductances that support neuronal rhythmicity. Thus, the data suggest that the mechanisms by which Shox2 INs sustain the locomotor rhythm throughout postnatal maturation are dynamic.

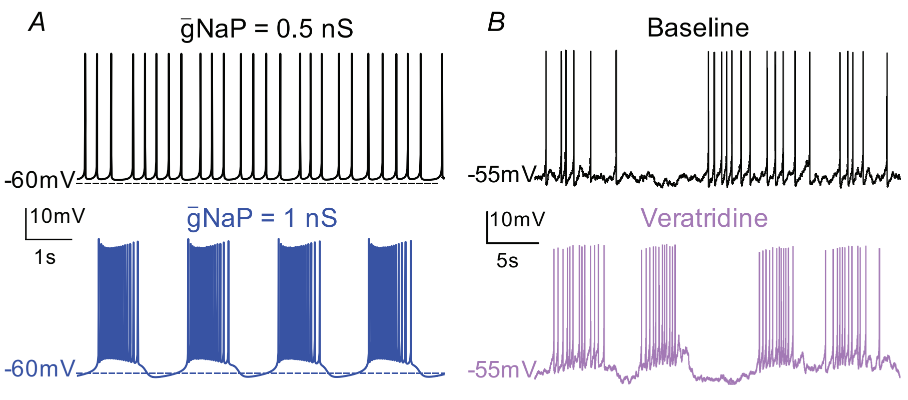


**Figure 8. Emergence of rhythmic bursting activity via amplification of $I_{NaP}$**
*A*, simulation of a single Shox2 IN. Increasing $\bar{g}_{NaP}$ from 0.5 to 1 nS converts tonic spiking to bursting. Model parameters: $\bar{g}_{NaP}$ = 220 nS, $\bar{g}_{Kdr}$ = 150 nS, $\bar{g}_M$ = 0.8 nS, $\bar{g}_{CaL}$ = 0.5 nS, $\bar{g}_{KCa}$ = 2 nS, $T_{hNaP}$ = 22 s. *B*, an example of a transition in an adult (P123) Shox2 IN from tonic to rhythmic burst firing after application of veratridine. [Colour figure can be viewed at wileyonlinelibrary.com]

## Rhythmogenic currents gain strength with age

We report that the prevalences of RNA in Shox2 INs for $Na_V1.6$ and $Ca_V1.3$ and the prevalences of $K_V7.2/3$ in Shox2 INs do not change developmentally. The lack of change in RNA expression was unexpected because it has been shown that voltage-gated ion channel expression does increase developmentally by P18 in motor neurons (Jiang, et al., 1999b). However, our data are consistent with the lack of change in the prevalences of currents with age. We were limited in our ability to characterize the membrane expression of channels which could contribute to PICs in Shox2 INs. This is because the concentrations of channels within axon initial segments in the case of $Na_V1.6$ (Drouillas et al., 2023) or distal dendrites for $Ca_V1.3$ (Ballou et al., 2006; Carlin et al., 2000) are difficult to detect in Shox2 neurons in that they do not have a common orientation and levels of tdTomato marker labelling were low beyond the soma. Our aim in the present study was to show that Shox2 INs express channels that are responsible for both sodium and calcium components of PICs observed with the electrophysiology results. We restricted our channel-specific examinations to the channel subunits most probably contributing to PICs (Drouillas et al., 2023; Jiang, et al., 1999b; Katz et al., 2018). However, there are likely to be other specific voltage-gated ion channels contributing to PICs in these neurons. These include $Na_V1.1$ (Drouillas et al., 2023) and $Ca_V1.2$ (Jiang, et al., 1999b) for $I_{NaP}$ and $I_{CaL}$, respectively. Further studies with targeted pharmacology and histology will reveal the extent to which combinations of these channels comprise PICs in Shox2 INs. In the present study, we saw modest attenuation of PICs in Shox2 INs after application of riluzole or nimodipine, which is not directly compatible with our RNAscope finding of high prevalences of $Na_V1.6$ $RNA^+$ and $Ca_V1.3$ $RNA^+$ Shox2 INs. However, it is plausible that not all RNA transcripts undergo translation into protein and that not all proteins are then trafficked to the neuronal membrane where they could contribute to the PICs measured and manipulated in the present study (Solé & Tamkun, 2020). Although RNA levels are consistent, the developmental increases in PIC and $I_M$ magnitudes may be caused by changes in the localization and/or density of the respective voltage-gated ion channels on the Shox2 IN membrane with age. Future studies aimed at the precise identities and locations of these channels may uncover how these intrinsic properties develop with finer precision.

In the cases of PICs which persist onto the descending phase of the voltage ramp and sAHP, the developmental shifts are distinct in that these properties are largely absent from Shox2 INs from neonatal mice. The increase in PIC magnitude with development matches the higher prevalence of PICs that persist onto the descending phase of the voltage ramp in juvenile and adult age groups because a larger amplitude PIC probably persists for longer during the voltage ramp protocol. This shift may also be explained by higher PIC-related channel expression in the membrane with age, which has yet to be examined and cannot be assessed by labelling RNA. It may also be explained by a change in channel composition contributing to PICs because other channels such as $Na_V1.1$ and $Ca_V1.2$ may differentially contribute to PICs in Shox2 INs throughout development. In the case of sAHP, it is clear that the neonatal Shox2 INs do not yet express SK2 and SK3 with high prevalence. The shape of action potentials including the afterhyperpolarization is known to dramatically change with age as a result of changes in voltage-gated ion channels (Abbinanti et al., 2012). This has been shown across development in V2a INs (Husch et al., 2015), which partially overlap with the Shox2 population (Dougherty et al., 2013). Furthermore, neonatal V2a INs have been shown to lack biphasic AHP compared to adult V2a INs (Husch et al., 2015). In Shox2 INs, this biphasic AHP appears at P10, a timepoint that may be consistent with the maturation of descending input to lumbar circuitry (Ballion et al., 2002; Pearlstein, 2013; Vinay et al., 2002) and is well-aligned with the establishment of weight-bearing locomotion and maturation of gait (Jiang, et al., 1999a).

## Potential to sculpt rhythmic firing behaviour

To date, examinations of identified spinal IN types that extend into adulthood are limited. We show that voltage-gated currents in Shox2 INs gain strength with age, and that Shox2 INs from juvenile and adult mice are more heterogenous than those from neonatal mice. A limitation of our study is that we did not assess how the morphology of Shox2 INs changed with post-natal development, which could have implications for ion channel distribution as well as space clamp errors in electrophysiological recordings (Sun et al., 2017). Future studies including perforated patch recordings and more detailed anatomical examinations may lead to better estimations of the values of key neuronal conductances and their distribution, as well as to determination of whether morphological changes correlate with the electrophysiological changes reported. The significant developmental change in input capacitance reported here may also be corroborated with detailed anatomical studies in the future. The increases in current densities with age in Shox2 INs may have an influence on the membrane time constant and both the input resistance and input capacitance. Overall, the data presented here suggests that the intrinsic mechanisms employed by Shox2 INs to shape their function are dynamic across development.

Both $I_T$ and $I_A$ may play more pronounced roles in mature Shox2 INs. However, these currents are difficult to isolate without pharmacology because of their similar voltage-dependent properties (Huguenard et al., 1991). It is known that specific ionic conductances contribute to rhythmogenic neuronal oscillations in many CPGs. Sodium-mediated PICs (Zhong et al., 2007; Ziskind-Conhaim et al., 2008), $I_T$ (Anderson et al., 2012; Ziskind-Conhaim et al., 2008) and $I_H$ (Chalif et al., 2022) have been considered essential for pharmacologically-evoked fictive locomotor activity to occur in the neonatal spinal cord, and $I_M$ has been shown to alter locomotion in juvenile rats such that their speed is significantly limited (Verneuil et al., 2020). It is possible that these currents have frequency-dependent properties in Shox2 INs, which may contribute to changes in membrane resonance thereby generating a functional rhythm (Matsumoto-Makidono et al., 2016). Although $I_T$ is only found in a subset of Shox2 INs from adult mice, it may still play a pronounced role in the rhythmogenic subset of Shox2 INs in adulthood. Interestingly, in reduced spinal cord preparations from P11–12 mice, an age where evoking coordinated motor activity *in vitro* is difficult, blockade of SK-mediated conductances promotes fictive locomotor activity (Mahrous & Elbasiouny, 2018). This suggests that the appearance of sAHP in a subset of mature Shox2 INs is not directly oscillation-promoting, although it may play a more nuanced role in shaping Shox2 IN firing behaviour in that subset. In the present dataset, no Shox2 INs showed robust spontaneous oscillations, potentially as a result of insufficient persistent sodium conductance because simulations suggested and experiments demonstrated that enhancement of this conductance led to oscillations in Shox2 INs. Previous studies suggest that the intrinsic bursting in a small number of neurons in the network (even 5%) may be sufficient to drive synchronous rhythmic activity in the network (Feldman and del Negro, 2006; Purvis et al., 2007). Our modelling data suggest that interactions of these ionic currents, specifically with $I_{NaP}$, shape oscillations of single neurons, which can be tested in the future during spontaneous or evoked oscillations in Shox2 INs.

In Shox2 INs from adult mice, it is still unclear which combination(s) of electrophysiological properties are essential for rhythmogenesis. In invertebrates including crabs (Golowasch & Marder 1992) and lobsters (Zhang et al., 2003), pacemaker neurons employ many of the conductances found in Shox2 INs, highlighting the roles that these properties can play in endogenous rhythmicity. These properties may be tightly linked in their influence on rhythmic bursting, which has been demonstrated in the case of $I_H$ and $I_A$ in the lobster (Zhang et al., 2003) and suggested in the case of PICs and $I_M$ in rodents (Verneuil et al., 2020). There are probably many overlapping combinations of the conductances included in this study that may each lead to rhythmic firing in Shox2 INs within different contexts of locomotor behaviours. This has been thoroughly described in identified neuron types within other organisms and contexts (Alonso & Marder, 2020). The clustering that we report in this study begins to highlight distinct features of Shox2 INs from juvenile and adult postnatal ages in which locomotor circuitry and behaviour is mature. Clusters 4–8, entirely comprised of juvenile and adult Shox2 INs, are characterized by the presence of slowly inactivating PICs observed in the descending phase of the ramp, the presence of sAHP and relatively increased current densities. This suggests that these properties may play a role in the mature functioning of Shox2 INs within locomotor circuitry. Furthermore, the post-neonatal increase in heterogeneity signifies that the processes promoting rhythmic bursting in subsets of these mature Shox2 INs are likely to be dynamic, in conjunction with synaptic connections, as previously suggested by modelling studies in other neuron types (Jasinski et al., 2013).

The subset of Shox2 INs linked to rhythm generation (Chx10$^-$) in the neonatal mouse is ~25% of the Shox2 IN population (Dougherty et al., 2013), and whether similarly sized clusters or current prevalences correspond to this subset remains to be determined. Determining whether the population size or electrophysiological profile of this rhythmogenic subset expands in the adult animal requires further experimentation. Nevertheless, mature Shox2 INs likely utilize the voltage-gated conductances, in some combination(s), including those found in this study, during rhythmic locomotor activity. Our single neuron models predict an interplay between conductances found in Shox2 INs across postnatal development. Perhaps this allows Shox2 INs to shape bursting behaviour in context-dependent manners. Such redundancies, or degeneracies, may lend to the robustness and resilience of Shox2 INs in mature mice as they traverse different biological contexts (Calabrese & Marder, 2024). Further studies are necessary to pinpoint how each of these voltage-sensitive properties can shape, mediate or dampen rhythmic firing in mature Shox2 INs.

## References

Abbinanti, M. D., Zhong, G., & Harris-Warrick, R. M. (2012). Postnatal emergence of serotonin-induced plateau potentials in commissural interneurons of the mouse spinal cord. *Journal of Neurophysiology*, **108**(8), 2191–2202.

Alonso, L. M., & Marder, E. (2020). Temperature compensation in a small rhythmic circuit. *eLife*, **9**, 1–24.

Amir, R., Michaelis, M., & Devor, M. (1999). Membrane potential oscillations in dorsal root ganglion neurons: Role in normal electrogenesis and neuropathic pain. *The Journal of Neuroscience*, **19**(19), 8589–8596.

Anderson, T. M., Abbinanti, M. D., Peck, J. H., Gilmour, M., Brownstone, R. M., & Masino, M. A. (2012). Low-threshold calcium currents contribute to locomotor-like activity in neonatal mice. *Journal of Neurophysiology*, **107**(1), 103–113.

Ballou, E. W., Smith, W. B., Anelli, R., & Heckman, C. J. (2006). Measuring dendritic distribution of membrane proteins. *Journal of Neuroscience Methods*, **156**(1–2), 257–266.

Ballion, B., Branchereau, P., Chapron, J., Vialá, D. V., & Vialá, V. (2002). Ontogeny of descending serotonergic innervation and evidence for intraspinal 5-HT neurons in the mouse spinal cord. *Developmental Brain Research*, **137**(1), 81–88.

Bertho, M., Caldeira, V., Hsu, L. J., Löw, P., Borgius, L., & Kiehn, O. (2024). Excitatory spinal Lhx9-derived interneurons modulate locomotor frequency in mice. *Journal of Neuroscience*, **44**(18), e1607232024.

Borowska, J., Jones, C. T., Deska-Gauthier, D., & Zhang, Y. (2015). V3 interneuron subpopulations in the mouse spinal cord undergo distinctive postnatal maturation processes. *Neuroscience*, **295**, 221–228.

Brocard, C., Plantier, V., Boulenguez, P., Liabeuf, S., Bouhadfane, M., Viallat-Lieutaud, A., Vinay, L., & Brocard, F. (2016). Cleavage of $Na^+$ channels by calpain increases persistent $Na^+$ current and promotes spasticity after spinal cord injury. *Nature Medicine*, **22**(4), 404–411.

Brocard, F., Shevtsova, N. A., Bouhadfane, M., Tazerart, S., Heinemann, U., Rybak, I. A., & Vinay, L. (2013). Activity-dependent changes in extracellular $Ca^{2+}$ and $K^+$ reveal pacemakers in the spinal locomotor-related network. *Neuron*, **77**(6), 1047–1054.

Brown, D. A., & Adams, P. R. (1980). Muscarinic suppression of a novel voltage-sensitive K+ current in a vertebrate neurone. *Nature*, **283**(5748), 673–676.

Brownstone, R. M., & Wilson, J. M. (2008). Strategies for delineating spinal locomotor rhythm-generating networks and the possible role of Hb9 interneurones in rhythmogenesis. *Brain Research Reviews*, **57**(1), 64–76.

Bywater, R. A. R., Small, R. C., & Taylor, G. S. (1989). Neurogenic slow depolarizations and rapid oscillations in the membrane potential of circular muscle of mouse colon. *The Journal of Physiology*, **413**(1), 505–519.

Calabrese, R. L., & Marder, E. (2024). Degenerate neuronal and circuit mechanisms important for generating rhythmic motor patterns. *Physiological Reviews*, **105**(1), 95–135.

Carlin, K. P., Jones, K. E., Jiang, Z., Jordan, L. M., & Brownstone, R. M. (2000). Dendritic L-type calcium currents in mouse spinal motoneurons: Implications for bistability. *European Journal of Neuroscience*, **12**(5), 1635–1646.

Cazalets, J.-R., Borde, M., & Claracl, F. (1996). The synaptic drive from the spinal locomotor network to motoneurons in the newborn rat. *The Journal of Neuroscience*, **16**(1), 298–306.

Chalif, J. I., Martínez-Silva, M. de L., Pagiazitis, J. G., Murray, A. J., & Mentis, G. Z. (2022). Control of mammalian locomotion by ventral spinocerebellar tract neurons. *Cell*, **185**(2), 328–344.e26.

Chang, Q., Gonzalez, M., Pinter, M. J., & Balice-Gordon, R. J. (1999). Gap junctional coupling and patterns of connexin expression among neonatal rat lumbar spinal motor neurons. *The Journal of Neuroscience*, **19**(24), 10813–10828.

Cowley, K. C., & Schmidt, B. J. (1997). Regional distribution of the locomotor pattern-generating network in the neonatal rat spinal cord. *Journal of Neurophysiology*, **77**(1), 247–259.

Crone, S. A., Quinlan, K. A., Zagoraiou, L., Droho, S., Restrepo, C. E., Lundfald, L., Endo, T., Setlak, J., Jessell, T. M., Kiehn, O., & Sharma, K. (2008). Genetic ablation of V2a ipsilateral interneurons disrupts left-right locomotor coordination in mammalian spinal cord. *Neuron*, **60**(1), 70–83.

Crone, S. A., Zhong, G., Harris-Warrick, R., & Sharma, K. (2009). In mice lacking V2a interneurons, gait depends on speed of locomotion. *Journal of Neuroscience*, **29**(21), 7098–7109.

Dai, Y., & Jordan, L. M. (2010). Multiple patterns and components of persistent inward current with serotonergic modulation in locomotor activity-related neurons in Cfos-EGFP mice. *Journal of Neurophysiology*, **103**(4), 1712–1727.

Danner, S. M., Shevtsova, N. A., Frigon, A., & Rybak, I. A. (2017). Computational modeling of spinal circuits controlling limb coordination and gaits in quadrupeds. *eLife*, **6**, e31050.

Deardorff, A. S., Romer, S. H., Deng, Z., Bullinger, K. L., Nardelli, P., Cope, T. C., & Fyffe, R. E. W. (2013). Expression of postsynaptic $Ca^{2+}$-activated $K^+$ (SK) channels at C-bouton synapses in mammalian lumbar $\alpha$-motoneurons. *The Journal of Physiology*, **591**(4), 875–897.

Dougherty, K. J., & Ha, N. T. (2019). The rhythm section: An update on spinal interneurons setting the beat for mammalian locomotion. *Current Opinion in Physiology*, **8**, 84–93.

Dougherty, K. J., Zagoraiou, L., Satoh, D., Rozani, I., Doobar, S., Arber, S., Jessell, T. M., & Kiehn, O. (2013). Locomotor rhythm generation linked to the output of spinal Shox2 excitatory interneurons. *Neuron*, **80**(4), 920–933.

Drouillas, B., Brocard, C., Zanella, S., Bos, R., & Brocard, F. (2023). Persistent Nav1.1 and Nav1.6 currents drive spinal locomotor functions through nonlinear dynamics. *Cell Reports*, **42**(9), 113085.

Feldman, J. L. (1986). Neurophysiology of breathing in mammals. In *Handbook of Physiology - The Nervous System IV*, 463–524.

Feldman, J. L., & del Negro, C. A. (2006). Looking for inspiration: New perspectives on respiratory rhythm. *Nature Reviews Neuroscience*, **7**(3), 232–241.

Garcia-Ramirez, D. L., Ha, N. T., Bibu, S., Stachowski, N. J., & Dougherty, K. J. (2021). Spinal cord injury alters spinal Shox2 interneurons by enhancing excitatory synaptic input and serotonergic modulation while maintaining intrinsic properties in mouse. *The Journal of Neuroscience*, **41**(27), 5833–5848.

Garcia-Ramirez, D. L., Singh, S., McGrath, J. R., Ha, N. T., & Dougherty, K. J. (2022). Identification of adult spinal Shox2 neuronal subpopulations based on unbiased computational clustering of electrophysiological properties. *Frontiers in Neural Circuits*, **16**, 957084.

Golowasch, J., & Marder, E. (1992). Ionic currents of the lateral pyloric neuron of the stomatogastric ganglion of the crab. *Journal of Neurophysiology*, **67**(2), 318–331.

Gong, S., Zheng, C., Doughty, M. L., Losos, K., Didkovsky, N., Schambra, U. B., Nowak, N. J., Joyner, A., Leblanc, G., Hatten, M. E., & Heintz, N. (2003). A gene expression atlas of the central nervous system based on bacterial artificial chromosomes. *Nature*, **425**(6961), 917–925.

Greene, D. L., Kang, S., & Hoshi, N. (2017). XE991 and linopirdine are state-dependent inhibitors for Kv7/KCNQ channels that favor activated single subunits. *Journal of Pharmacology and Experimental Therapeutics*, **362**(1), 177–185.

Ha, N. T., & Dougherty, K. J. (2018). Spinal Shox2 interneuron interconnectivity related to function and development. *eLife*, **7**, e42519.

Harris-Warrick, R. M. (2002). Voltage-sensitive ion channels in rhythmic motor systems. *Current Opinion in Neurobiology*, **12**(6), 646–651.

Harris-Warrick, R. M. (2010). General principles of rhythmogenesis in central pattern generator networks. *Progress in Brain Research*, **187**, 213–222.

Hinckley, C. A., Wiesner, E. P., Mentis, G. Z., Titus, D. J., & Ziskind-Conhaim, L. (2010). Sensory modulation of locomotor-like membrane oscillations in Hb9-expressing interneurons. *Journal of Neurophysiology*, **103**(6), 3407–3423.

Huguenard, J. R., Coulter, D. A., & Prince, D. A. (1991). A fast transient potassium current in thalamic relay neurons: Kinetics of activation and inactivation. *Journal of Neurophysiology*, **66**(4), 1304–1315.

Husch, A., Dietz, S. B., Hong, D. N., & Harris-Warrick, R. M. (2015). Adult spinal V2a interneurons show increased excitability and serotonin-dependent bistability. *Journal of Neurophysiology*, **113**(4), 1124–1134.

Jasinski, P. E., Molkov, Y. I., Shevtsova, N. A., Smith, J. C., & Rybak, I. A. (2013). Sodium and calcium mechanisms of rhythmic bursting in excitatory neural networks of the pre-bötzinger complex: A computational modelling study. *European Journal of Neuroscience*, **37**(2), 212–230.

Jiang, Z., Carlin, K. P., & Brownstone, R. M. (1999a). An in vitro functionally mature mouse spinal cord preparation for the study of spinal motor networks. *Brain Research*, **816**(2), 493–499.

Jiang, Z., Rempel, J., Sawchuk, M. A., Carlin, K. P., & Brownstone, R. M. (1999b). Development of L-type calcium channels and nifedipine sensitive motor activity in the postnatal mouse spinal cord. *European Journal of Neuroscience*, **11**(10), 3481–3487.

Katz, E., Stoler, O., Scheller, A., Khrapunsky, Y., Goebbels, S., Kirchhoff, F., Gutnick, M. J., Wolf, F., & Fleidervish, I. A. (2018). Role of sodium channel subtype in action potential generation by neocortical pyramidal neurons. *Proceedings of the National Academy of Sciences of the United States of America*, **115**(30), E7184–E7192.

Kjaerulff, O., & Kiehn, O. (1996). Distribution of networks generating and coordinating locomotor activity in the neonatal rat spinal cord In vitro: A lesion study. *The Journal of Neuroscience*, **16**(18), 5777–5794.

Köhler, M., Hirschberg, B., Bond, C. T., Kinzie, J. M., Marrion, N. V., Maylie, J., & Adelman, J. P. (1996). Small conductance, calcium-activated potassium channels from mammalian brain. *Science*, **273**(5282), 1709–1714.

Madisen, L., Zwingman, T. A., Sunkin, S. M., Oh, S. W., Zariwala, H. A., Gu, H., Ng, L. L., Palmiter, R. D., Hawrylycz, M. J., Jones, A. R., Lein, E. S., & Zeng, H. (2010). A robust and high-throughput cre reporting and characterization system for the whole mouse brain. *Nature Neuroscience*, **13**(1), 133–140.

Mahrous, A. A., & Elbasiouny, S. M. (2018). Modulation of SK channels regulates locomotor alternating bursting activity in the functionally-mature spinal cord. *Channels*, **12**(1), 9–14.

Marder, E., & Calabrese, R. L. (1996). Principles of rhythmic motor pattern generation. *Physiological Reviews*, **76**(3), 687–717.

Matsumoto-Makidono, Y., Nakayama, H., Yamasaki, M., Miyazaki, T., Kobayashi, K., Watanabe, M., Kano, M., Sakimura, K., & Hashimoto, K. (2016). Ionic basis for membrane potential resonance in neurons of the inferior olive. *Cell Reports*, **16**(4), 994–1004.

McCrea, D. A., & Rybak, I. A. (2008). Organization of mammalian locomotor rhythm and pattern generation. *Brain Research Reviews*, **57**(1), 134–146.

Oswal, A., Brown, P., & Litvak, V. (2013). Synchronized neural oscillations and the pathophysiology of Parkinson's disease. *Current Opinion in Neurology*, **26**(6), 662–670.

Pearlstein, E. (2013). Role of descending aminergic pathways in the development of locomotion. *Current Pharmaceutical Design*, **19**(24), 4332–4340.

Purvis, L. K., Smith, J. C., Koizumi, H., & Butera, R. J. (2007). Intrinsic bursters increase the robustness of rhythm generation in an excitatory network. *Journal of Neurophysiology*, **97**(2), 1515–1526.

Rivera-Arconada, I., Roza, C., & Lopez-Garcia, J. A. (2013). Characterization of hyperpolarization-activated currents in deep dorsal horn neurons of neonate mouse spinal cord in vitro. *Neuropharmacology*, **70**, 148–155.

Rybak, I. A., Dougherty, K. J., & Shevtsova, N. A. (2015). Organization of the mammalian locomotor CPG: Review of computational model and circuit architectures based on genetically identified spinal interneurons. *ENeuro*, **2**(5), ENEURO.0069-15.2015.

Rybak, I. A., Paton, J. F., & Schwaber, J. S. (1997). Modelling neural mechanisms for genesis of respiratory rhythm and pattern. I. Models of respiratory neurons. *Journal of Neurophysiology*, **77**(4), 1994–2006.

Rybak, I. A., Shevtsova, N. A., Ptak, K., & McCrimmon, D. R. (2004). Intrinsic bursting activity in the pre-bötzinger complex: Role of persistent sodium and potassium currents. *Biological Cybernetics*, **90**(1), 59–74.

Rybak, I. A., Shevtsova, N. A., St-John, W. M., Paton, J. F., & Pierrefiche, O. (2003). Endogenous rhythm generation in the pre-bötzinger complex and ionic currents: Modelling and in vitro studies. *European Journal of Neuroscience*, **18**(2), 239–257.

Sharples, S. A., & Miles, G. B. (2021). Maturation of persistent and hyperpolarization-activated inward currents shapes the differential activation of motoneuron subtypes during postnatal development. *eLife*, **10**, 71385.

Solé, L., & Tamkun, M. M. (2020). Trafficking mechanisms underlying Nav channel subcellular localization in neurons. In *Channels* (Vol. **14**, Issue 1, pp. 1–17). Taylor and Francis Inc.

Spencer, N. J., Hibberd, T. J., Travis, L., Wiklendt, L., Costa, M., Hu, H., Brookes, S. J., Wattchow, D. A., Dinning, P. G., Keating, D. J., & Sorensen, J. (2018). Identification of a rhythmic firing pattern in the enteric nervous system that generates rhythmic electrical activity in smooth muscle. *The Journal of Neuroscience*, **38**(24), 5507–5522.

Sun, M. Y., Chisari, M., Eisenman, L. N., Zorumski, C. F., & Mennerick, S. J. (2017). Contributions of space-clamp errors to apparent time-dependent loss of Mg2+ block induced by NMDA. *Journal of Neurophysiology*, **118**(1), 532–543.

Talpalar, A. E., Bouvier, J., Borgius, L., Fortin, G., Pierani, A., & Kiehn, O. (2013). Dual-mode operation of neuronal networks involved in left–right alternation. *Nature*, **500**(7460), 85–88.

Verneuil, J., Brocard, C., Trouplin, V., Villard, L., Peyronnet-Roux, J., & Brocard, F. (2020). The M-current works in tandem with the persistent sodium current to set the speed of locomotion. *PLoS Biology*, **18**(11), e3000738.

Vinay, L., Brocard, F., Clarac, F., Norreel, J.-C., Pearlstein, E., & Pflieger, J.-F. (2002). Development of posture and locomotion: An interplay of endogenously generated activities and neurotrophic actions by descending pathways. *Brain Research Reviews*, **40**(1–3), 118–129.

Wang, F., Flanagan, J., Su, N., Wang, L. C., Bui, S., Nielson, A., Wu, X., Vo, H. T., Ma, X. J., & Luo, Y. (2012). RNAscope: A novel in situ RNA analysis platform for formalin-fixed, paraffin-embedded tissues. *Journal of Molecular Diagnostics*, **14**(1), 22–29.

Wang, H.-S., Pan, Z., Shi, W., Brown, B. S., Wymore, R. S., Cohen, I. S., Dixon, J. E., & Mckinnon, D. (1998). KCNQ2 and KCNQ3 potassium channel subunits: Molecular correlates of the M-channel. *Science*, **282**(5395), 1890–1893.

Zhang, Y., Oliva, R., Gisselmann, G., Hatt, H., Guckenheimer, J., & Harris-Warrick, R. M. (2003). Overexpression of a hyperpolarization-activated cation current (Ih) channel gene modifies the firing activity of identified motor neurons in a small neural network. *Journal of Neuroscience*, **23**(27), 9059–9067.

Zhong, G., Masino, M. A., & Harris-Warrick, R. M. (2007). Persistent sodium currents participate in fictive locomotion generation in neonatal mouse spinal cord. *The Journal of Neuroscience*, **27**(17), 4507–4518.

Ziskind-Conhaim, L., Mentis, G. Z., Wiesner, E. P., & Titus, D. J. (2010). Synaptic integration of rhythmogenic neurons in the locomotor circuitry: The case of Hb9 interneurons. *Annals of the New York Academy of Sciences*, **1198**(1), 72–84.

Ziskind-Conhaim, L., Wu, L., & Wiesner, E. P. (2008). Persistent sodium current contributes to induced voltage oscillations in locomotor-related Hb9 interneurons in the mouse spinal cord. *Journal of Neurophysiology*, **100**(4), 2254–2264.

## Additional information

### Competing interests

The authors declare that they have no competing interests.

### Author contributions

SS, NAS, IAR and KJD conceptualized the study. SS performed the electrophysiology experiments. SS and LY performed the histology experiments. SS and KJD analyzed the data. NAS and IAR performed modelling and simulations. SS, NAS, IAR and KJD wrote the manuscript with input from all authors.

### Funding

This work was supported by National Institutes of Health grants R01 NS130799 (KJD, IAR), T32 NS121768 (SS) and F31 NS132514 (SS).

### Acknowledgements

We thank members of the Marion Murray Spinal Cord Research Centre and Drexel ULAR for support, and we also thank Ron Harris-Warrick, Jenna McGrath, Arron Hall and Leonardo Garcia-Ramirez for comments on an earlier version of the manuscript.

### Keywords

interneuron, ionic currents, locomotion, rhythm generation, spinal cord

## Supporting information

Additional supporting information can be found online in the Supporting Information section at the end of the HTML view of the article. Supporting information files available:

**Peer Review History**